

2015

Clinical Probe Utilizing Surface-Enhanced Raman Scattering (SERS) for In-Situ Molecular Imaging Applications

Jeonghwan Kim

Louisiana State University and Agricultural and Mechanical College, kjeong2@tigers.lsu.edu

Follow this and additional works at: https://digitalcommons.lsu.edu/gradschool_dissertations



Part of the [Electrical and Computer Engineering Commons](#)

Recommended Citation

Kim, Jeonghwan, "Clinical Probe Utilizing Surface-Enhanced Raman Scattering (SERS) for In-Situ Molecular Imaging Applications" (2015). *LSU Doctoral Dissertations*. 3642.

https://digitalcommons.lsu.edu/gradschool_dissertations/3642

This Dissertation is brought to you for free and open access by the Graduate School at LSU Digital Commons. It has been accepted for inclusion in LSU Doctoral Dissertations by an authorized graduate school editor of LSU Digital Commons. For more information, please contact gradetd@lsu.edu.

CLINICAL PROBE UTILIZING
SURFACE-ENHANCED RAMAN SCATTERING (SERS) FOR
IN-SITU MOLECULAR IMAGING APPLICATIONS

A Dissertation

Submitted to the Graduate Faculty of the
Louisiana State University and
Agricultural and Mechanical College
in partial fulfillment of the
requirements for the degree of
Doctor of Philosophy

in

Division of Electrical and Computer Engineering
The School of Electrical Engineering and Computer Science

by

Jeonghwan Kim

B.Eng., Kyungwon University (Now Known As Gachon University), 2007

M.S., Louisiana State University, 2011

August 2015

ACKNOWLEDGEMENTS

This research was financially supported in part by National Institutes of Health (NIH - R03EB012519-01A1) and the majority of this work has performed through Electronic Material Device Laboratory (EMDL), at Electrical Engineering Department. Some processing equipment have been supported by Center for Advanced Microstructures and Devices (CAMD), Louisiana State University (LSU).

I would like to express my gratitude to all people who have supported my Ph.D. dissertation. First of all, I want to deeply thank my Ph.D. advisor, Dr. Martin Feldman for all advice, guidance, and encouragement throughout this work. He has provided an unique opportunity for me to enrich my knowledge in the areas of applied optics and micro-electro-mechanical systems (MEMS) and have encouraged me personally in many matters. Also, I would like to express gratitude to the committee members, Dr. Theda Daniels-Race, Dr. Georgios Veronis, Dr. Kidong Park, and Dr. Laura Ikuma for their interest and valuable suggestions.

I am grateful to Dr. Dooyoung Hah for the opportunity of this research project to me. Special thanks go to Dr. Yoonyoung Jin and Dr. Kyung-Nam Kang who provided encouragement and support. I would like to thank Dr. Junseo Choi and Dr. Edward Song for allowing technical facilities. I am also thankful to my group members: Dr. Daniel Herbert, Mr. Sean Hou, and Ms. Srismrita Basu for all their help and Mr. Christopher E O'Loughlin at EMDL for material and equipment advice. I would like to acknowledge Mr. Kalyan Kanakamedia and Ms. Madhavi Divakar for the atomic force microscopy (AFM) scans. All these people have provided assistance to this work, so I am also grateful to them.

Above all, I am truly grateful to my parents and the family of my older brother for their limitless faith and love. Without their spiritual support, this work would not have accomplished.

TABLE OF CONTENTS

ACKNOWLEDGEMENTS		ii
LIST OF TABLES		v
LIST OF FIGURES		vi
ABSTRACT		x
CHAPTER 1.	INTRODUCTION	1
1.1.	Molecular Imaging Technology	1
1.1.1.	Principle of Modalities	2
1.2.	Raman Scattering	8
1.3.	Surface-Enhanced Raman Scattering (SERS)	11
1.4.	Surface-Enhanced Raman scattering (SERS) Substrates	14
CHAPTER 2.	RESEARCH MOTIVATION AND GOAL	16
2.1.	Research Motivation	16
2.2.	Research Goal	18
CHAPTER 3.	EXPERIMENT SETUP	20
3.1.	Porous Silicon Substrate Preparation	20
3.1.1.	Porous Silicon	20
3.1.2.	Wet Etching	25
3.1.3.	Wet and Dry Etching	27
3.2.	Nanostructure Replication from Porous Silicon	29
3.2.1.	Gold Deposition as Releasing Layer	30
3.2.2.	Epoxy Casting	30
3.3.	Measurement Setup of Surface-Enhanced Raman Scattering (SERS)	32
CHAPTER 4.	TRANSPARENT SURFACE-ENHANCED RAMAN SCATTERING SUBSTRATE CHARACTERIZATION	35
4.1.	Different Gold Thickness Deposition	35
4.2.	Background Raman Signals	37
4.3.	Target Material Preparation	39
4.3.1.	Rhodamine 6G (R6G)	39
4.3.2.	Gelatin with Rhodamine 6G (R6G)	39
4.4.	Reflection and Transmission of Nanorough Gold in Fluidic Cell	41
CHAPTER 5.	REMOTE RAMAN	49
5.1.	Photon Transmission	49
5.2.	Probe Head Design	52

CHAPTER 6.	APPLICATIONS FOR BIOLOGICAL SPECIMEN; CHICKEN CARTILAGE	63
CHAPTER 7.	SUMMARY, CONCLUSION AND FUTURE WORK	70
7.1.	Summary and Conclusion	70
7.2.	Future Work	72
REFERENCES	74
APPENDIX A.	PERMISSION TO REPRINT COPYRIGHTED MATERIAL	82
APPENDIX B.	PERMISSION TO REPRINT COPYRIGHTED MATERIAL	83
APPENDIX C.	PERMISSION TO REPRINT COPYRIGHTED MATERIAL	84
APPENDIX D.	PERMISSION TO REPRINT COPYRIGHTED MATERIAL	85
VITA	86

LIST OF TABLES

1.1	The comparison of advantages and limitations between molecular imaging technology and typical <i>in vitro</i> technology.	1
1.2	Different localized surface plasmon resonance wavelength ranges of gold (Au), silver (Ag), and copper (Cu) for SERS substrates.	14
3.1	Porous silicon (PS) types depending on pore diameter.	23
3.2	Effects with increasing factors on porous silicon formation such as doping type, HF concentration, current density, and processing time.	24

LIST OF FIGURES

1.1	The schematic of computed tomography (CT).	3
1.2	The schematic of magnetic resonance imaging (MRI).	4
1.3	The schematic of ultrasound instrument.	5
1.4	The schematics of (a) positron emission tomography (PET) and (b) single photon emission computed tomography (SPECT).	7
1.5	The schematic of optical bioluminescence imaging.	8
1.6	Two types of scatterings: Rayleigh and Raman scattering with Stoke and anti-Stoke.	9
1.7	Two images show (a) the schematic of the normal Raman spectroscopy and (b) LABRAM Integrated Raman Spectroscopy System at EMDL, LSU.	10
1.8	The charge transferring schematic in the chemical enhancement mechanism of the SERS cross-section.	13
1.9	Various nanostructures of SERS substrates: (a) metal nanoparticle film, (b) metal-coated nanosphere structure, (c) metal-coated random nanostructure, and (d) metal-coated patterned nanostructure.	15
3.1	The cross-sectional view of porous silicon formation. Porous structures are formed under an electrolyte, and the structures are also separated from bulk silicon at the bottom.	20
3.2	The mechanism of porous silicon formation. (a) Si atom is bonded with two H atoms at the surface, (b) Si-H bonds are replaced by Si-F due to the nucleophilic attack of the fluoride ions, (c) another F ⁻ is attracted and replaces Si-H into Si-F bond, (d) HF attacks the rest of the Si-Si backbonds, and (e) SiF ₄ molecules are formed, and eventually react with another HF in order to further stabilize the formation of SiF ₆ ²⁻	22
3.3	The pores in the highly doped p-type silicon wafer have no branches and show concave interface between the porous structures and the bulk silicon substrate.	25
3.4	Schematic of an anodization cell.	26
3.5	Images of (a) electrochemically etched porous silicon and (b) SEM at the center of the sample.	27

3.6	Images contains (a) wet and dry etched porous silicon in the circle and also only dry etch silicon outside of circle, (b) SEM image at the center of wet and dry etched area.	28
3.7	The schematic comparison between (a) before and (b) after the dry etching with 45° angled SEM images.	29
3.8	(a) Illustration of nanostructure casting steps and (b) images of cast epoxy from porous silicon which has nanostructures inside of a quarter circle.	31
3.9	Typical Surface-Enhanced Raman Scattering (SERS) measurement methods including (a) drop and dry, (b) flowing target molecule with SERS active nanometallic particles, and (c) target molecule flowing over SERS active area.	33
3.10	The schematic of (a) fluidic cell parts including different sized glass slides, metal tube with 1 mm outer diameter, and wooden block, (b) a direction of injecting target analyte into fluidic cell, and (c) zoomed active area having several layers containing nanorough gold on epoxy.	34
4.1	Different additional gold thicknesses (20 nm, 50 nm, and 80 nm) on cast epoxy from wet and dry etched silicon.	36
4.2	UV curable epoxy is cast from (a) dry etched area, and (b) both wet and dry etched area, and 60 nm of gold is deposited on (a) and (b).	36
4.3	AFM images of 40 nm gold on epoxy substrates casting from (a) only dry etched region and (b) both wet and dry etched region. The roughness of two regions are compared within the scanned 1 μm range. The RMS roughness is 14 nm on only the dry etched region and 32 nm on the both wet and dry etched region.	37
4.4	All background spectra involved in the fluidic cell development. Particularly, epoxy shows the highest spectrum, but the overall peaks are not overlapped with the peak of a target molecule, Rhodamine 6G.	38
4.5	Chemical structure of Rhodamine 6G.	39
4.6	Different concentrations of Rhodamine 6G solutions.	40
4.7	Gelatin with different concentrations of Rhodamine 6G.	40
4.8	Raman signals from 80 nm of gold in contact with the Rhodamine 6G solutions which concentrations ranging from 1 mM to 1 nM.	42

4.9	Raman signals from 1 nM to 1 mM R6G on 80 nm gold on three types of substrates. The intensities of the Raman signals was obtained at the 1362 cm ⁻¹ and signals from both etches shows the highest signals. The dotted curve shows shifted peaks in spectrum below 1 μM R6G solution on the substrate with no etch.	43
4.10	Surface-Enhanced Raman spectra on the cast epoxy substrate with no etching of the silicon wafer.	44
4.11	Surface-Enhanced Raman signals with additional gold on the epoxy casting from both wet and dry etched silicon wafer. The cast substrates with 20 nm gold and no additional gold can only detect R6G signals above the concentration of 10 μM.	45
4.12	Surface-Enhanced Raman signals with additional gold on the epoxy casting from dry etched only silicon wafer. The cast substrates with 20 nm gold and no additional gold can only detect R6G signals above the concentration of 10 μM.	46
4.13	Transmission of Surface-Enhanced Raman signals from epoxy casting from both wet and dry etched silicon with different gold thickness.	47
4.14	Transmission of Surface-Enhanced Raman signals from epoxy casting from only dry etched silicon with different gold thickness.	48
5.1	The schematic of the remote Raman apparatus with the top view.	51
5.2	The schematic of light propagation in (a) π/4 and (b) π/2 gradient-index (GRIN) lenses.	53
5.3	The first probe head is assembly with the GRIN lens and the SERS substrate in the housing. The GRIN lens is positioned with the screw and the SERS substrate is attached to the grass for the first design.	54
5.4	The remote Raman spectrum of the mixture (5 ml of 1 mM of Rhodamine 6G and 1 g of the gelatin) is measured under the initial remote Raman apparatus. ...	54
5.5	The experimental test of the GRIN lens focusing distance depending on the epoxy Thickness.	57
5.6	The reflected laser beam from the gold surface makes the best focus with the distance of approximately 35.31 mm between the second lens and the first surface of GRIN lens.	58
5.7	(a) A photograph of the improved probe and (b) the laser focusing with the probe tip positons.	59

5.8	Schematic drawing for numerical calculation of laser beam propagation in (a) parallel and (b) with a slope through $\pi/2$ GRIN lens with 5.2 mm in length and 1 mm in radius.	60
5.9	Numerical model of epoxy thickness depending on the air gap.	61
5.10	(a) photograph of the improved probe injected into a gelatin block mixed with a 1 mM Rhodamine 6G solution, and (b) Raman spectrum of 1 mM Rhodamine 6G through the probe and the articulated arm.	62
6.1	Raman spectrum of (a) human cartilage and (b) human bone is corresponding to the measured Raman spectrum of (c) chicken cartilage and (b) chicken bone with 50x microscope objective and 5 seconds integration time.	64
6.2	Three cartilages are prepared with (a) hypertonic saline, (b) hypotonic saline and (c) isotonic saline, and Raman spectra are measured with 50x microscope objective and 5 seconds integration time.	65
6.3	Chicken cartilage after sanding with 10 μm grits in order to make the top surface flat.	66
6.4	Comparison (a) without and (b) with sputtered gold on sanded cartilage.	67
6.5	Probe measurement with 30 nm nanorough gold against the chicken cartilage on the stage of Raman spectrometer.	69
7.1	The processing flow for the transparent SERS substrate.	71

ABSTRACT

In this research, a clinical probe utilizing Surface-Enhanced Raman Scattering (SERS) is developed for molecular imaging application which is a visualizing technology to support early diagnosis by providing images in molecular level. In addition to other molecular imaging applications using magnetic resonance, light, and ultrasound, Raman spectroscopy has great potential in terms of non-invasiveness, safety, imaging agent-free, and scanning multiple molecules at a time. However, the critical limitation of Raman spectroscopy using *in-vivo* molecular imaging application is the inherent low sensitivity of Raman effect. The challenge is overcome by employing SERS enhancing Raman scattering with concentrated electromagnetic oscillation in nanometallic structures. This phenomenon gives normal Raman spectroscopy more capabilities for diverse applications, especially for a clinical Raman probe of molecular imaging.

The imaging apparatus is composed of three parts: SERS substrate with nanostructures, probe with gradient-index (GRIN) lens, and signal transmission system from the spectrometer and the probe. For a transparent SERS substrate, electrochemically etched porous silicon (PS) is employed as a master mold from which a transparent UV epoxy is cast, and different thicknesses of gold (Au) are sputtered over the cast nanostructures. Rhodamine 6G solutions on the transparent SERS substrates are characterized and analyzed with various aspects in a fluidic cell.

In addition to the transparent SERS substrate, a clinical probe is customized with the optical analysis of gradient-index (GRIN) lens in order to focus laser beam on SERS substrate. A transmission system, called “articulated arm” is built with multiple rotating joints which reflect laser light 90 degree. The clinical probe is assembled with transmission system, and the scanned Raman signals are transmitted from the target specimen to the Raman spectrometer. Some measurement results of a gelatin block contains Rhodamine 6G demonstrate that the developed

remote probe using SERS and articulated arm show promising remote Raman detections for molecular imaging applications.

CHAPTER 1. INTRODUCTION

1.1. Molecular Imaging Technology

Molecular imaging technology covers visualizations as well as characterizations of biological and biochemical procedures at molecular and cellular levels in living creatures without any damage. The technology has been developed since the 1980s and is currently becoming more attractive to diverse biomedical areas, because it moves from *in vitro* diagnosis to *in-vivo* detection [1]. This means that people are interested in studying molecular organization, interaction, and the formation or elimination within cells. It is obvious that molecular imaging technology is able to provide a valuable in addition to the study of biological phenomena, pathology, progress mechanism of disease, and drug development in research [2]. In addition, molecular imaging has kept improving with the necessities of early detection, precise diagnosis, and surgical guidance in medicine because internal diseases including gastric cancer and other biopsies are not easy for detection at the early stages [3]. The other advantages in molecular imaging technology are real time, non-invasive, rapid, and efficient analysis and diagnosis [4, 5]. Thus, it has considerable to

Table 1.1. The comparison of advantages and limitations between molecular imaging technology and typical *in vitro* technology. After references [6]

	Molecular Imaging Technology	Typical <i>in vitro</i> Technology
Visualization	Good	Bad
Repeatability	Good	Relatively bad
Real time/ Dynamic detection	Good	Bad
Non-invasiveness	Good	Variable
Cost/Availability	Relatively high	Low
Imaging agent	Required	Not required

to improve the fields of diagnostics, medical treatment, and drug discovery and development. The advantages and challenges of the molecular imaging technology can be summarized by comparing it to typical *in vitro* technology in shown Table 1.

1.1.1. Principle of Modalities

Molecular imaging technology can be viewed in three different perspectives: the method of using energies including X-rays, positrons, photons, sound waves, spatial resolutions including macroscopic, mesoscopic, and microscopic, and information types including anatomical/structural and molecular/cellular. The overview of molecular imaging technology is going to be briefly explained by the informational perspective [5, 7].

According to the informational perspective, molecular imaging technology separates into two modalities: anatomical/structural and molecular/cellular information. Anatomical/structural imaging information is detected by structural changes such as computed tomography (CT) [8], magnetic resonance imaging (MRI) [8, 9], and ultrasound [10]. Molecular/cellular imaging information is detected by molecular/cellular changes such as positron emission tomography (PET) [11], single photon emission computed tomography (SPECT) [12], optical imaging [5], and Surface-Enhanced Raman Scattering (SERS) [13, 14].

Computed tomography (CT) is similar to two-dimensional (2-D) X-ray imaging and it can also provide three-dimensional (3-D) images. The meaning of the word “tomography” comes from the combination of Greek words. “Tomo” and “graphy” which translates to, “slice” and “drawing.” Thus, CT is able to produce 3-D anatomical images of tissues in living subjects by employing X-ray absorption. CT is composed of three parts: X-ray tube as a source, detector as a receiver, and scanner bed as a sample loading stage depicted in Fig. 1.1. The X-ray tube and detector are located in the same axis but are attached to a circular ring against each other. In the circular ring, there is

a scanner bed and the ring rotates around in the direction of the bed. When the CT operates, the fan beam is generated by the X-ray tube and is simultaneously measured by the detector during a scan. The scanned image is then interpreted as white, black, or other various contrasts. White means high absorption of X-ray by tissues and bones, whereas black means low absorption of X-ray by the air. The other various contrasts yield different detailed images. CT is commonly employed for research and clinic because of high spatial resolution, limitless penetration depth, and good temporal resolution. However, it also has some shortcomings regarding low sensitivity, low resolution for soft tissues, limitations of molecular imaging applications, ionizing radiation, and limitations of number of scans.

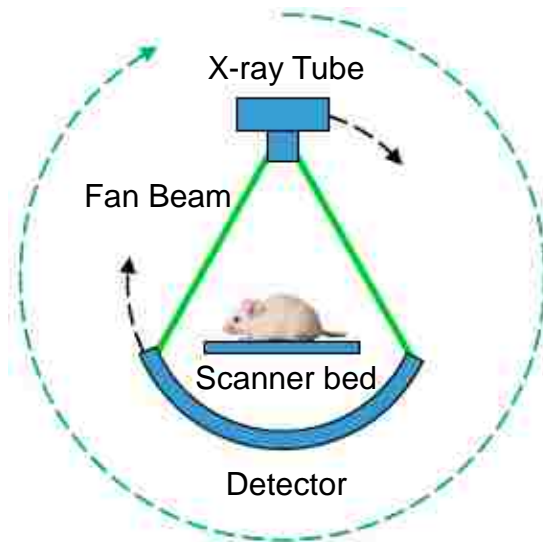


Fig. 1.1. The schematic of computed tomography (CT). After references [6]

MRI is one of the more powerful scanning tools using the energy of strong magnetism and radiofrequency (RF) for tomographic images of living subjects [9]. As shown in Fig. 1.2, the scanner is operated by three coils. The largest coil mostly generates uniform magnetic fields. The gradient coil, the second largest, moves the source of MR signals due to the generation of diverse

magnetic fields in all X, Y, and Z axes. The RF coil, the smallest of the three, generates an RF pulse that changes magnetic dipole alignment. In theory, it is the same as nuclear magnetic resonance (NMR) which use hydrogen atoms for living subject imaging [15]. Atoms are composed of nucleons and electrons. The nucleus is separated into protons and neutrons which spin about their axes. The existence of atomic angular momentum is dependent upon the quantitative balance of protons and neutrons in an atom. If they are balanced, the net angular momentum is zero, but they generate an angular momentum with odd number of protons and neutrons in nuclei. In nature, the angular momentum causes a magnetic field by the proton mass, spin, and charge. This generated magnetic field is called a magnetic momentum. It is known that the ratio of angular momentum and magnetic momentum is referred as gyromagnetic ratio, which is particularly important for magnetically active nuclei. Hydrogen (^1H) is the most dominant element in the human body for magnetically active nuclei, and there are also some others including carbon (^{13}C), oxygen (^{17}O), fluorine (^{19}F), sodium (^{23}Na), and phosphorus (^{31}P). MRI has many advantages of having limitless depth of penetration, quantitative data, and no ionizing radiation, whereas it also presents the disadvantages of poor sensitivity, no cost effectiveness, and inconvenience.

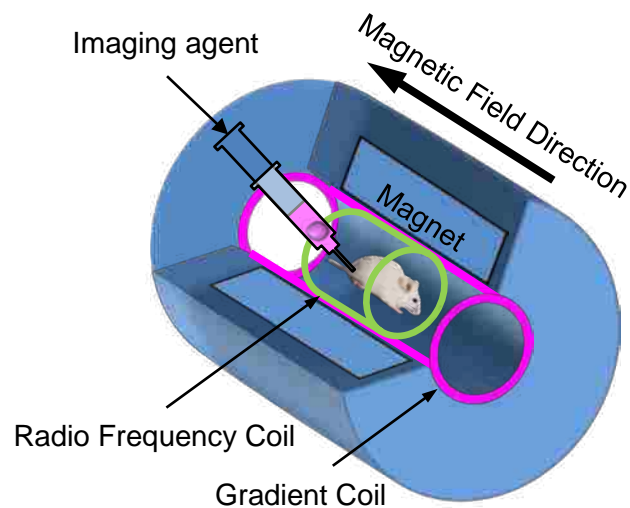


Fig. 1.2. The schematic of magnetic resonance imaging (MRI). After references [6]

Ultrasound is also commonly employed for diagnostic and clinical purposes. The instrument is basically composed of a probe, a probe controller, and an imaging system as shown in Fig. 1.3. The probe has two functions: a transducer and a receiver. When the transducer transmits high frequency sounds, ranging from 1 MHz to 20 MHz, into a living subject, some sounds bounce back to the transducer [16]. The reflected sound frequencies show different properties compared to the transmitted frequency. The reflected sound wave to the receiver is eventually converted back into the electrical signal. Finally, the converted electrical signals are visualized on a screen through the image processing system. The ultrasound has the benefits of cost effectiveness and portability and it is relatively safe because of no ionizing radiation. However, it has the weakness of having limited penetration depth and it only shows basic anatomical information. The spatial resolutions of ultrasound ranges from 10 μm to 100 μm

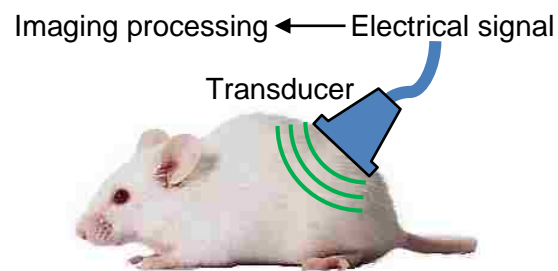


Fig. 1.3. The schematic of ultrasound instrument. After references [6]

which are not suitable for good molecular imaging, and ultrasound also needs a coupling of instrument to the subject [17].

PET and SPECT are the major nuclear imaging technologies which use radioactive substances in order to detect any changes in the living subjects at the molecular level. They have significant advantages including no penetration depth for scanning and excellent sensitivity for the

clinical purpose [18]. The image of PET goes through a computer processing step by using radiolabelled imaging agent for a particular target molecule. The imaging agent is injected into living subjects and they are specifically concentrated into a target such as cancer and tumor as depicted on the left schematic in Fig. 1.4 (a). If the nucleus of the imaging agent possesses surplus protons it becomes unstable. The nucleus can be stabilized by changing the proton into a neutron, a positron, and a neutrino as the agent emits positron over time which is known as beta-plus decay. The emitted positron moves less than 1 mm, and it is reacted with the electron of a living subject, called annihilation. A pair of positron and electron generates two photons having 511 keV in energy with 180° in the opposite direction [11]. SPECT on the right in Fig. 1.4 (b) is very similar to the PET in terms of using radioactive substances for tomographic images. Conventional gamma camera provides 2-D image with radioactive substances, but SPECT generates a 3-D image with multiple shots of the gamma camera by a computer processing technique. The main difference between SPECT and PET is that SPECT directly measures the gamma rays from the radioactive substances, but PET measures gamma rays from the annihilation between the positron and the electron. Thus, SPECT has a lower resolution than the PET. In terms of cost effectiveness, SPECT is better than PET, however both are still relatively expensive compared with other imaging methods. Moreover, SPECT provides more information for a given image, since it allows the injection of more than two radioisotopes with labelling [18].

Optical imaging is also one of the molecular imaging technologies, and it has been studied for the basic imaging research and clinical diagnosis for a long time. Optical imaging has improved for scanning the entire human body because of the limitless penetration depth. In general, the optical imaging is divided into fluorescence and bioluminescence imaging. Fluorescence imaging

uses light energy absorption with external illumination in a certain wavelength, and fluorochrome, one of fluorescent chemical compounds, is employed to visualize molecular images such as

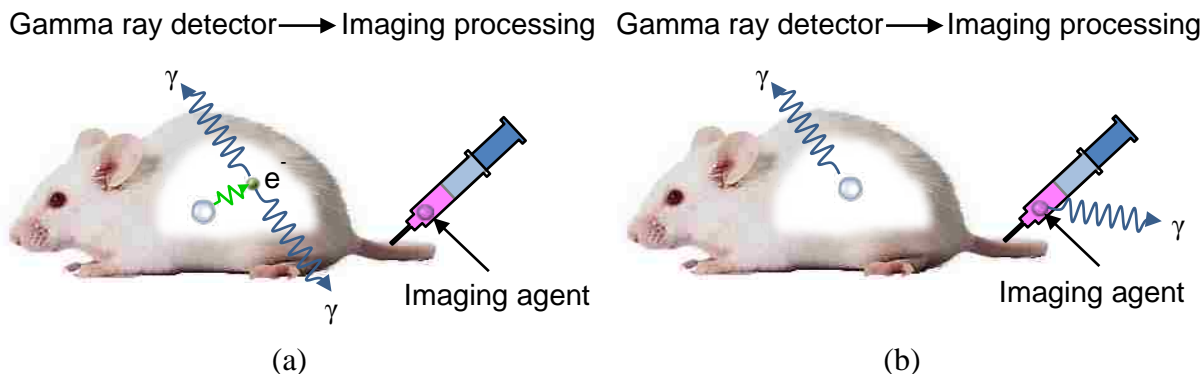


Fig. 1.4 The schematics of (a) positron emission tomography (PET) and (b) single photon emission computed tomography (SPECT). After references [6]

encoded fluorescence reporters and fluorescence-tagged molecules [19]. On the other hand, bioluminescence in Fig. 1.5 does not require external light sources, because it utilizes chemiluminescent reactions between enzymes and their substrates, for instance, luciferase and D-luciferin respectively. The enzyme oxidizes the substrate under the existence of adenosinetriphosphate and oxygen, and the reaction emits the yellow/green color light at 575 nm in wavelength [20]. The benefits of bioluminescence are lower background signals and higher sensitivity because of weak inherent bioluminescence of tissues and enzymatic signal amplifications for *in-vivo* detection, respectively. The issue of fluorescence imaging is that fluorescence light can only be detected in the range of 600 nm to 800 nm of the wavelength, because hemoglobin and water, a primary element of tissue, absorb light that is out of the range of the fluorescence lights [21].

SERS is one of the new emerging modalities for molecular imaging technology. SERS has been developed based on regular Raman spectrum, so it has become a new type of powerful tool

for bioresearch and clinical use. In order to understand SERS, Raman effect must be addressed, and more detailed information of SERS given in the following subchapters.

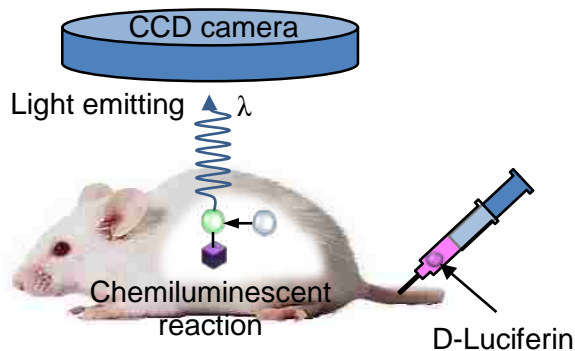


Fig. 1.5 The schematic of optical bioluminescence imaging. After references [6, 22]

1.2.Raman Scattering

The Raman effect, also called Raman scattering, was discovered by C.V. Raman in 1928 [23], and awarded him Nobel Prize in Physics in 1930. The phenomena described one of the scattering lights. The scattered light is primarily divided into two categories as described in Fig. 1.6: Rayleigh and Raman scattering, or elastic and inelastic scattering, respectively. Rayleigh scattering has the same wavelength as the incident light, so it is observed in most of the scattered light. However, Raman scattering has different wavelength from the incident light, and is quite weak compared to the Rayleigh scattering. In addition, two types of Raman scattering can be observed: Stokes and anti-Stokes. The difference is that Stokes scattering produces lower energy light than the incident light, whereas the anti-Stokes scattering produces higher energy light.

The Raman scattering effect is employed in Raman spectroscopy which is a widely utilized spectroscopic technique. As shown in Fig. 1.7 (a), a modern spectrometer is composed of four major parts; a laser as a light source, sample illumination and light collection system, Rayleigh rejection filter/grating, and a charge coupled devices (CCD) as a detector. Also, the available

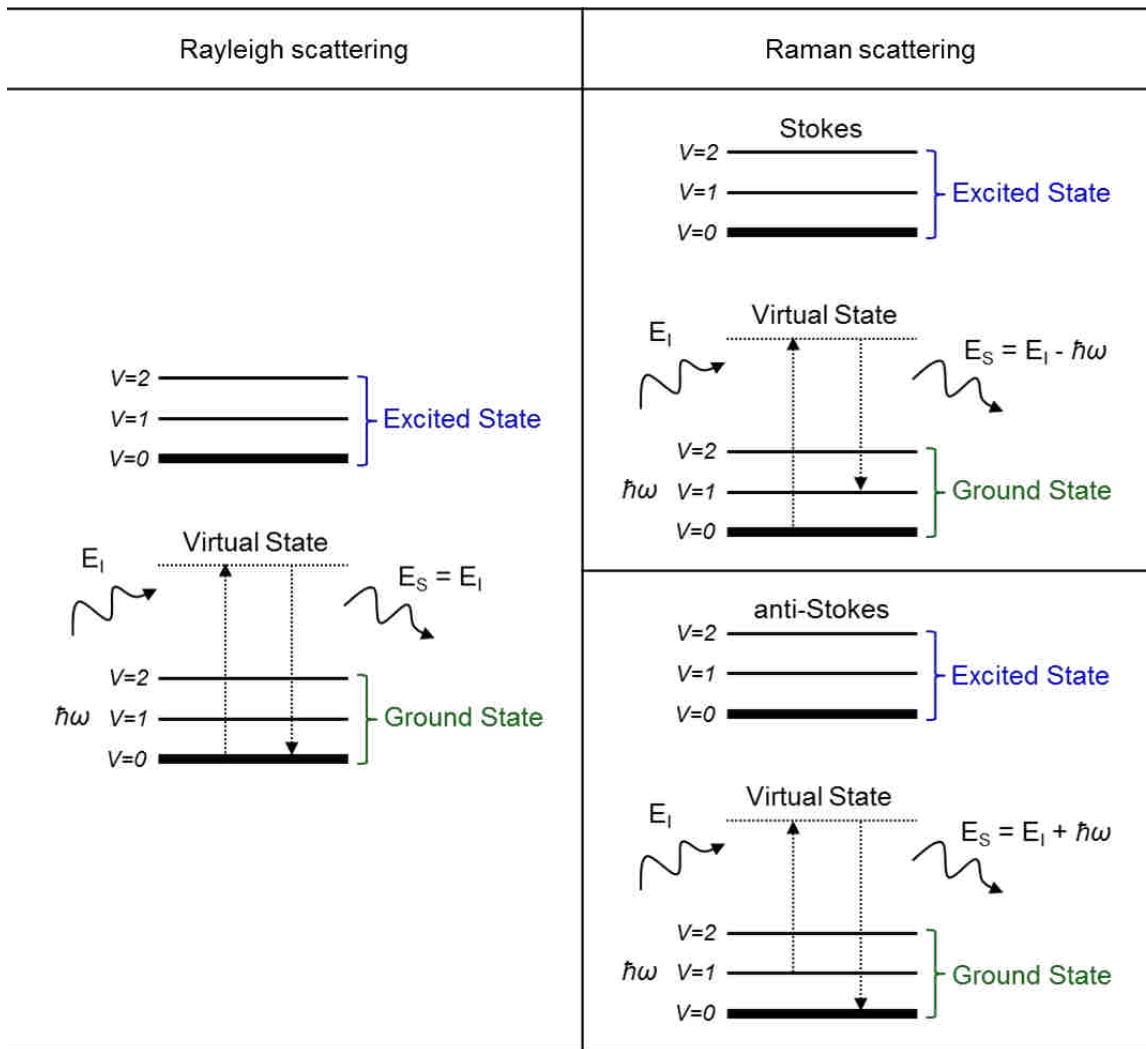


Fig. 1.6 Two types of scatterings: Rayleigh and Raman scattering with Stoke and anti-Stoke.
After references [24]

Raman spectroscopy at the EMDL, LSU is shown in Fig. 1.7 (b), which is comparable to the schematic. Raman spectroscopy is commonly used for biosciences, analytical chemistry, solid state physics, and other fields which need material characterization, because the measurement can usually be carried out both in solid and in liquid phase, and sample preparation time is shorter than for most other analysis tools. Also, it does not require a large quantity of sample volume, since the laser focused spot is in the micron scale range. In addition, Raman spectroscopy also has the merits

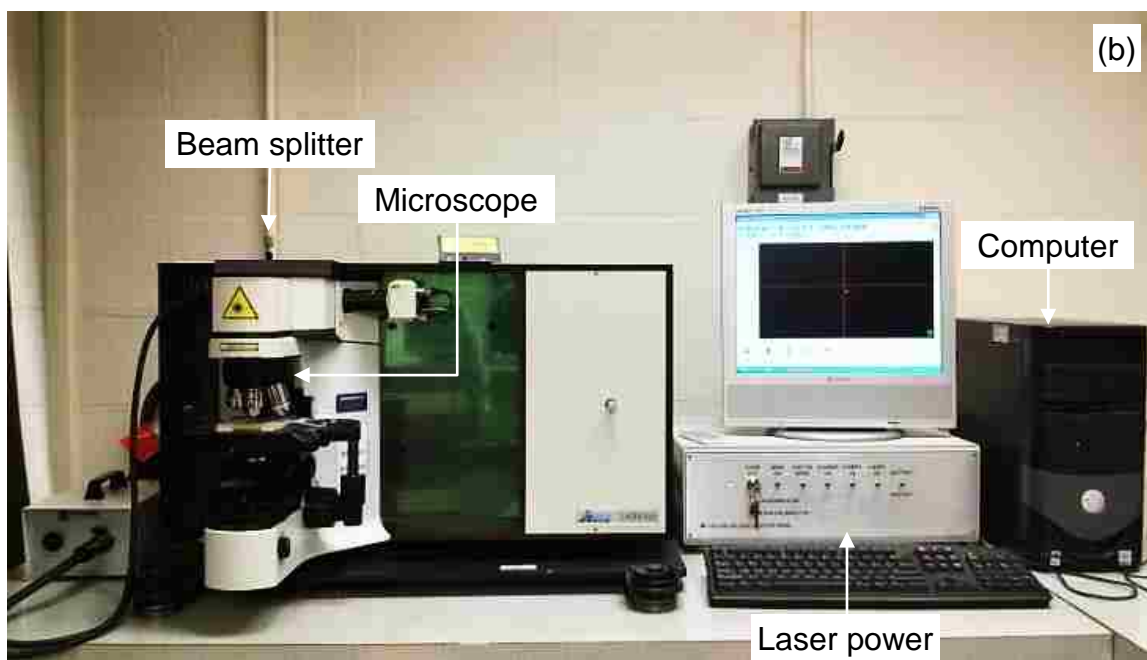
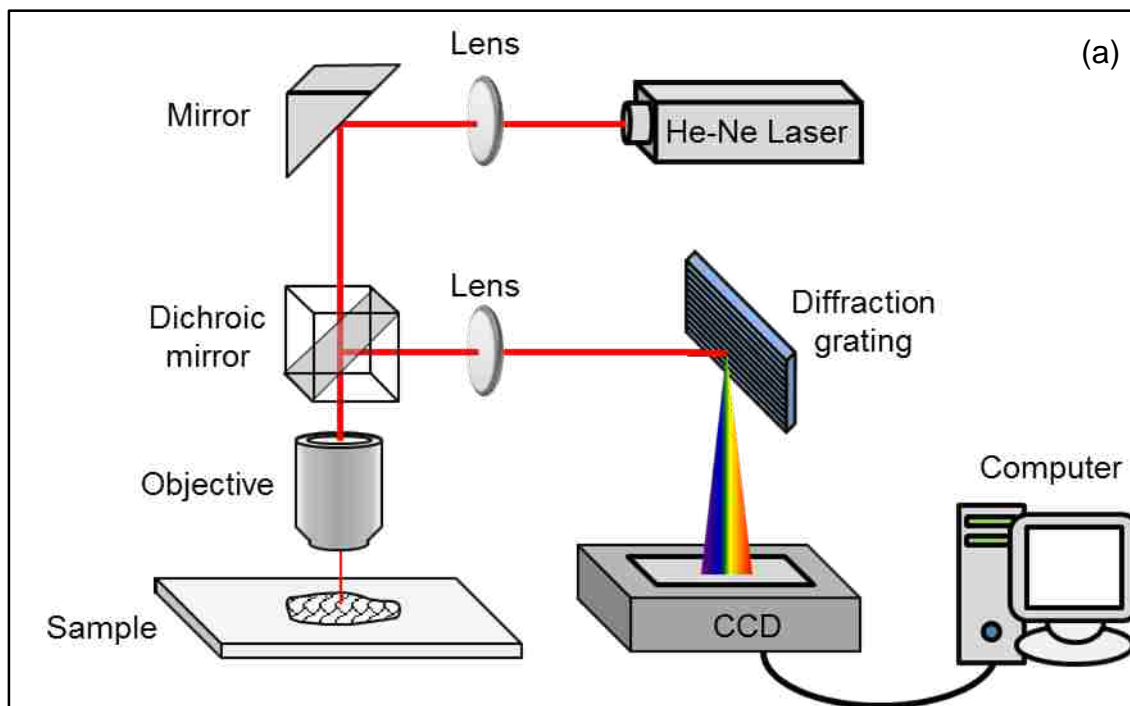


Fig. 1.7 Two images show (a) the schematic of normal Raman spectroscopy and (b) LABRAM Integrated Raman Spectroscopy System at EMDL, LSU.

of a non-destructive method and a short measurement time. However, it is necessary to improve the sensitivity, because Raman is relatively a weak effect. Thus, efforts have been made to increase the laser power in order to overcome the weak signal, but high laser power can sometimes destroy the biological samples.

1.3. Surface-Enhanced Raman Scattering (SERS)

Surface-Enhanced Raman Scattering (SERS) emerged in the 1970s [25] and has been intensively studied both theoretically and experimentally in order to overcome the inherently weak Raman effect [26]. Since the 1980s, various approaches have been applied including rough metallic surface [27], colloidal metal nanoparticles [28], metallic islands [29], and so on.

In principle, SERS employs surface plasmon resonance (SPR) which is a collective oscillation of electrons of the material by a radiated electromagnetic (EM) wave. It normally takes place in high conductive metals such as gold (Au), silver (Ag), and copper (Cu), because of many electrons on their surfaces. The SPR can be divided into two effects depending on the location of the plasmon [30]. If the plasmon propagates along the thin metallic surface, it is called, surface plasmon polaritons (SPPs.) The SPPs propagation distance is from tens to hundreds of micrometers in the plane (x- and y- direction), but SPPs do not exist in the z-direction. If the surface has nanostructures which are smaller than the wavelength of the incident light, surface plasmons with a certain frequency are trapped around the nanostructure, referred to as a local surface plasmon resonance (LSPR.) In terms of detection, surface plasmon resonance (SPR) is relatively easier because it shows large changes in refractive index rather than LSPR which EM field disappears in a very short range. However, in terms of intensity, LSPR has higher molecule densities than SPR in the same area, due to its unique nanometallic structures. It is believed that the Surface-Enhanced Raman Scattering (SERS) is mostly attributed by LSPR, depending on the nanostructural

dimension, shape, and distance between nanostructures. In addition, SERS has simultaneously improved by another enhancement mechanisms; chemical enhancement [30].

In summary, the EM enhancement mechanism is dominant in SERS effect and LSPR is the major contributor in the EM enhancement. The induced LSPR area between the nanometallic structures is called the SERS active site, and the intensive LSPR at the SERS active site is called “hot spot.” The enhancement factor by this mechanism is about 10^5 - 10^8 when the target molecules are close enough to the metallic surface within approximately tens of nanometer range. This means that the EM mechanism does not require that the analyte makes contact with the metal surface [31], and it has been shown that the distance between analyte and metal surface is a significant factor in SERS intensity (I_{SERS}) with the following equation;

$$I_{SERS} = \left(\frac{a+r}{a}\right)^{-10}$$

where a and r are the average dimension of nanostructure and the distance between analyte and nanostructure, respectively [32].

On the other hand, chemical enhancement is less significant in SERS effect and this enhancement is also called a “charge transfer” mechanism because it occurs when the molecule is adsorbed to the nanometallic structure. The adsorbed molecule and the metal surface make a covalently bonded complex which changes the Raman polarizability of the molecule. When the incident light exposes to the molecule and the metal surface, the electrons/holes in the metal are excited and inelastic tunneling of the electrons occurs to the lowest unoccupied molecular orbital (LUMO) of the adsorbed molecule. The electrons generate a Raman-shifted photon when the electrons are relaxed to where it was in the metal [33]. The illustration of Fig. 1.8 describes direct (1) and indirect (2 & 3) electron excitation with light exposure to the adsorbed molecule on the metal surface.

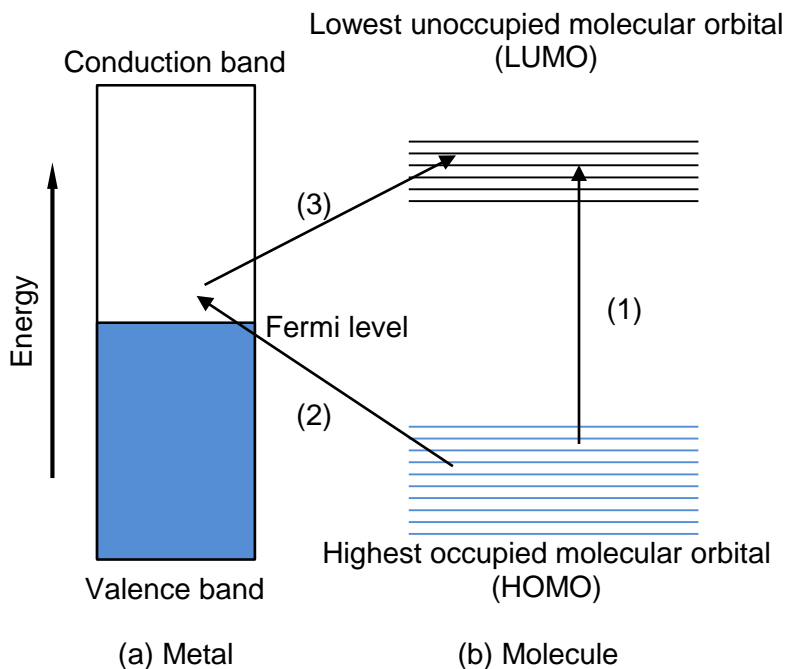


Fig. 1.8. The charge transferring schematic in the chemical enhancement mechanism of the SERS cross-section. After reference [24]

SERS happens with two mechanisms; electromagnetic and chemical mechanisms which are already explained. SERS enhancement factor (EF) simply can be calculated by the signal intensities and analyte concentrations. EF is described as the following equation

$$EF = \frac{I_{SERS} \cdot N_{Ref}}{I_{Ref} \cdot N_{SERS}}$$

where I_{SERS} is the enhanced Raman intensity and N_{SERS} is the number of molecules participated in the enhancement. I_{Ref} and N_{Ref} are representative to the non-enhanced Raman intensity and the involved molecule numbers for the I_{Ref} from the reference substrate, respectively [34].

1.4. Surface-Enhanced Raman scattering (SERS) Substrates

Many nano-sized geometries with metals such as gold (Au), silver (Ag), and copper (Cu) are potential candidates for the SERS substrates. Typically Au, Ag, and Cu are used for SERS substrate, because their wavelengths caused by localized surface plasmon resonances (LSPR), in the visible and near infrared range in Table 1.2, include useful Raman spectrum. However, Au and Ag are more commonly employed, since the optical properties and stabilities against air of these metals are superior to other metals [35, 36]. Au and Ag nanoparticles [37-40] synthesized from solutions are applied for SERS substrates as illustrated in Fig. 1.9 (a), because the metal nanoparticles are simple, low-cost in process, and demonstrate higher enhancement factors. However, nanoparticles have some drawbacks such as poor reproducibility due to the nanoparticle control limitation under liquid and nanoparticle agglomeration from high surface-to-volume ratio [41].

Table 1.2. Different localized surface plasmon resonance wavelength ranges of gold (Au), silver (Ag), and copper (Cu) for SERS substrates.

Metal	Wavelength Range [nm]
Gold (Au)	580 – 1250
Silver (Ag)	400 – 1000
Copper (Cu)	550 – 1250

Au and Ag also can be employed as a thin film by deposition over the nanostructure shown in Fig. 1.9 (b), (c), and (d). The method using metallic film is more reproducible, stable and controllable during fabrication, but it does not provide as high an enhancement effect as the nanoparticles in SERS. Researchers have categorized two types of nanostructures, one is randomly distributed nanostructures and the other is periodically arrayed nanostructures for SERS study.

Random nanostructures are defined as any nanostructures whose arrangement is random, so the nanostructures in a random array are rapidly fabricated with diverse ways in a large area [27, 42-44]. Randomly distributed nanostructures are effectively used for SERS substrate with ease and fast fabrication processes, but stability of SERS enhancement of the random structures is worse than the periodically arrayed structures. Thus, periodically ordered nanostructures provide more reliable SERS effect with various lithography technologies such as nanosphere lithography [45-47], focused ion beam (FIB) [48, 49], electron-beam (e-beam) lithography [50, 51] and nanoimprint lithography (NIL) [52-54]. The patterned template using lithography is quite reproducible and controllable even though it fabricates very small features in the few nanometer range.

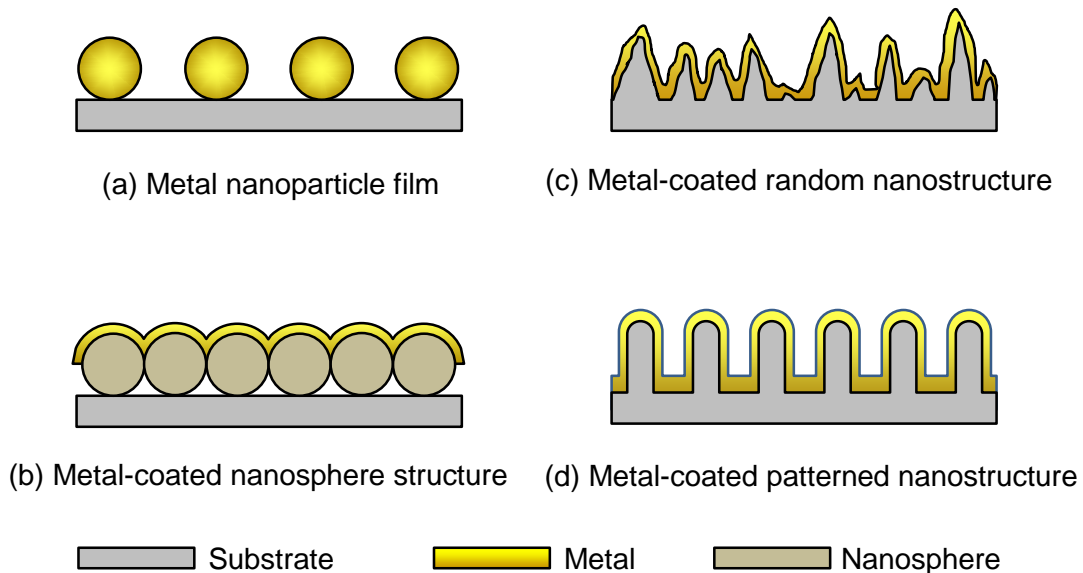


Fig. 1.9 Various nanostructures of SERS substrate: (a) metal nanoparticle film, (b) metal-coated nanosphere structure, (c) metal-coated random nanostructure, and (d) metal-coated patterned nanostructure. After reference [26]

CHAPTER 2. RESEARCH MOTIVATION AND GOAL

2.1 Research Motivation

Molecular imaging technologies are normally defined as real time and noninvasive visualizing systems of molecules or cells within living organisms, so they have become indispensable tools for not only early detection of molecular and cellular abnormalities for clinical applications, but also to enlighten intricate biochemical phenomena in research [55]. Modalities of molecular imaging technology include computed tomography (CT), magnetic resonance imaging (MRI), positron emission tomography (PET)/single photon emission tomography (SPECT), ultrasound, optical imaging, Surface-Enhanced Raman Scattering (SERS), and so on [7].

Even though current molecular imaging technologies are used in the clinics and research, they still need improvements as *in-vivo* molecular imaging for the following reasons. CT has a limitation in visualizing the molecular level imaging because of the low sensitivity of CT-compatible contrast agents. MRI also suffers from low sensitivity in molecular imaging beyond anatomical morphologies. Meanwhile, PET/SPECT can scan structures in molecular levels with relatively high sensitivity without any limitation of penetration depth, but the scanning time is limited by the radiation dose because of radionuclide imaging agent. Ultrasound also still needs to improve sensitivities for imaging molecules. Moreover, optical image using white light scattering relies on visualization of tissue deformation and color change, and fluorescent imaging requires a rapid photobleach of fluorescent molecules which limit detection sensitivity and research duration [7]. Because of the limitations in other imaging modalities, interest has moved to using Raman scattering as an alternative and an auxiliary method. Molecular imaging by employing Raman scattering is able to provide more accurate specificity based on molecular or cellular composition as a less invasive and label free technique. However, Raman scattering also has some challenges.

Raman scattering is weaker than fluorescence signal, so it has a relatively low efficiency. Raman spectrometer is also needed to improve the collection efficiency under short spectral acquisition time and the spectrum analysis from the unknown confound. In order to improve Raman scattering Surface-Enhanced Raman Scattering (SERS) was developed. SERS is able to provide the benefits of high sensitivity and good multiplex capabilities. Rough nanometallic features for SERS are able to increase the signal intensities by at least 10^6 times compared to the normal Raman scattering. The enhancement factors are divided into two mechanisms; one is electromagnetic enhancement and the other is chemical enhancement. The first mechanism is that if incident light hits a rough metallic surface the electromagnetic wave is amplified by the resonance of the localized surface plasmon resonance (LSPR) which enhancement factor is about 10^4 by the near field. The second mechanism is involved with the charge transfer between the molecule and the metal surface in the range of long field where the enhancement is approximately a factor of 10^2 . However, the enhancement factors are determined by dielectric environment, shapes, distances between nanostructures, and sizes of the nanostructures.

This research aims to develop a contact type clinical probe by employing SERS which is suitable for the detection of an early abnormal tissue by collecting quantitative information of the molecules and cells. This approach is comparable to the first successful *in-vivo* endoscope using colloidal gold (Au) nanoparticles in order to detect tumor in a mouse [56]. This research proposes that a contact type SERS probe which is composed of a SERS probe head, a light path media, a spectroscope, and a computer. This would become an attractive clinical probe for an early diagnostic assay.

2.2 Research Goal

This research describes clinical probe development utilizing a SERS substrate for contact detection. The designed probe can overcome the critical disadvantage of weak Raman signals for remote measurement with SERS substrate. The substrate needs to be transparent and biocompatible, so the illuminating laser is focused on the nanometallic surface through the substrate which is pressed against or inserted into the biological sample. Therefore, this proposed research deals with the development of transparent SERS substrate, clinical probe, and optical transmission system.

Firstly, a suitable transparent SERS substrate has to be developed for a probe head. Here, porous silicon (PS) is employed for building a SERS substrate. PS is a master mold in SERS substrate development. Some groups have used PS for SERS substrate because of its unique three-dimensional (3-D) structure [57-59], but it is rarely used as a master mold because of replication difficulties. For PS structure replication, ultraviolet (UV) curable epoxy is used because it is relatively hard, transparent and biocompatible compared to polydimethylsiloxane (PDMS). The process is very simple, cost effective, and short preparation time and the enhancement characteristics of the transparent SERS substrate are comparable in reflectance and transmission. The enhancement comparison provides more functional information for the SERS substrate before applying for a probe.

Secondly, a clinical Raman probe is built with the SERS substrate. The designed probe is composed of aluminum housing and stainless steel tube. Optical elements of small positive lens and GRIN lens with a transparent SERS substrate are implanted in the housing and stainless steel tube, respectively. Small GRIN lens is adopted for focusing the laser light through the transparent SERS substrate and the GRIN lens allows a narrow probe tip to minimize invasiveness.

Finally, a light transmission system is developed which is called “an articulated arm”. The key parts of the articulated arm are rotating joints with 45° angled mirrors. The probe is directly attached to the articulated arm which is also connected to the Raman spectrometer without the normal objective and the feasibility of the clinical Raman probe using SERS substrate is characterized through the articulated arm.

CHAPTER 3. EXPERIMENT SETUP

3.1. Porous Silicon Substrate Preparation

3.1.1. Porous Silicon

Hollow silicon structures are formed by electrochemical etching under hydrofluoric acid (HF) mixed with ethanol (EtOH). Cross sections of etched structures are vertically hollow dents, which are called porous silicon (PS) as illustrated in Fig. 3.1. Surface-to-volume-ratio is dramatically increased with morphological complexities, and unique porous structures have been used in many applications including gas sensors [60, 61], optical filters [62], solar cells [63], electronics [64], and biosensors [58, 65, 66].

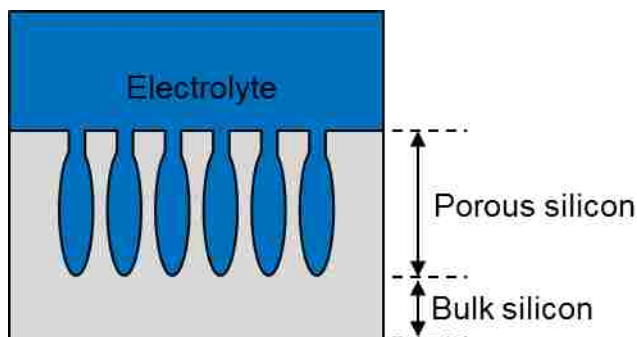


Fig. 3.1 The cross-sectional view of porous silicon formation. Porous structures are formed under an electrolyte, and the structures are also separated from bulk silicon at the bottom.

Uhlir and Turner [67, 68] first observed PS under some particular conditions during the electropolishing of silicon surfaces in the late 1950s. After it had been discovered, they believed that subfluoride $(\text{SiF}_2)_x$ was grown on the silicon surface by the electrochemical reaction. However,

several years later, it was proved that no subfluoride was grown during the anodic dissolution. Many researchers have proposed various theories regarding PS formations and morphologies. V. Lehmann and U. Gösele [69] have proposed one acceptable theory. Silicon (Si) atoms at the surface are bonded with two hydrogen (H) by weak polarization due to their similar electronegativity, so that the silicon surface is inert in the absence of the electronic holes (h^+) in Fig. 3.2 (a). However, if the hole gets to the silicon surface under an electric field, the Si-H bonds are replaced with a Si-F bond due to the nucleophilic attack of the fluoride ions (F^-) in Fig. 3.2. (b). One Si-F formation generates a polarization, and another F^- is attracted and replaces Si-H into Si-F bond as shown in Fig.3.2 (c). The presence of the Si-F bonds' polarization weakens the Si-Si backbonds with a low electron density, and therefore the HF attacks the rest of the Si-Si backbonds as indicated in Fig. 3.2 (d). During these steps, H_2 is generated and one electron is injected into the Si electrode. As a result, silicon tetrafluoride (SiF_4) molecules are formed at the silicon surface, and SiF_4 molecules eventually react with another HF molecule in order to further stabilize the hexafluorosilicate anions (SiF_6^{2-}) in Fig. 3.2 (e). Once one silicon atom is extracted from the surface, geometrical shapes of the silicon surface are also changed. Thus, the electric field distribution is highly focused in a trench, and the probability of the h^+ transfer is increased over other locations. According to this process, vertical etching is preferred than horizontal etching which causes many porous structures at the silicon surface.

PS can form quite versatile morphologies because of geometrical distributions on the surface. Pore dimensions, shapes, and orientations are the major factors changing the morphologies. It has been known that the orientation of the PS is quite dependent upon the orientation of silicon substrates. In this research, (100) silicon wafers, which make highly perpendicular pores against silicon surface, are used for electrochemical etching.

In a big picture, pores can be divided into three different categories depending on the pore diameters such as micro pores (less than 10 nm), meso pores (between 10 and 50 nm) and macro pores (larger than 50 nm) as shown in Table 3.1 [70] . Basically, modifications of pore diameters are dependent upon doping types and concentrations of silicon substrates, HF concentrations, current densities, and processing times. The relationships with increasing values of the parameters are summarized in Table 3.2.

Table 3.1. Porous silicon (PS) types depending on pore diameter.

Pore Diameter	Porous Silicon Type
< 10 nm	Micro/Nano pores
10 nm – 50 nm	Meso pores
> 50 nm	Macro pores

(1) Doping type and doping concentration

The pore sizes of p-type and n-type silicon are differently affected as the doping concentration increases. The porosity of the p-type silicon inversely decreases to the increase of the doping concentration, but the n-type silicon increases its porosity with an increase in the doping concentration. In both cases, however, the etch rate is increased as the doping concentration increases.

(2) Current density and HF concentration

When the current density increases, the pore size is also slightly increased in both p-type and n-type silicon. The electrolyte is a mixture of hydrofluoric acid (HF) and ethanol. HF is the main etching chemical in the electrolyte. As the HF concentration increases, the porosity is decreased. Ethanol in the electrolyte is used for two reasons: one is that alcohol provides good wettability against hydrophobic Si surface, so the electrolyte easily covers evenly through the small pores. The other is that ethanol is able to effectively eliminate H₂ bubbles from where the pores are formed. This is quite significant because, during the electrochemical etching, H₂ bubbles are generated as a by-product, which is likely to stay near the pore site and disturb the next pore formation. Thus, ethanol can be effective in forming a uniform pore creation by removing the bubbles [71].

Table 3.2 Effects with increasing factors on porous silicon formation such as doping type, HF concentration, current density, and processing time.

Increasing of	Porosity	Etching Rate
Doping (p-type)	Decrease	Increase
Doping (n-type)	Increase	Increase
HF Concentration	Decrease	Decrease
Current Density	Increase	Increase
Time	Slightly Increase	Decrease

Pores can be formed with or without the branches which is smaller pores formed from main pores. Pore branch creations depend on the doping concentration of the silicon substrate. Generally, branch formations in the p-type wafer are different from that in n-type silicon wafers. In p-type silicon wafers, more branches are observed in low doped silicon substrates. On the other hand, highly doped n-type wafers have more branches than the minimally doped ones. In this etching process, a highly doped p-type wafer is employed, and therefore the branches are seldom observed as shown in Fig. 3.3. In addition, when the PS is vertically etched from the bulk silicon substrate, the shapes of the interface between the PS and the bulk silicon substrate are highly concave and the depth difference of the concave between the center and the edge is tens of nanometers as evidenced by the SEM image in Fig. 3.3.

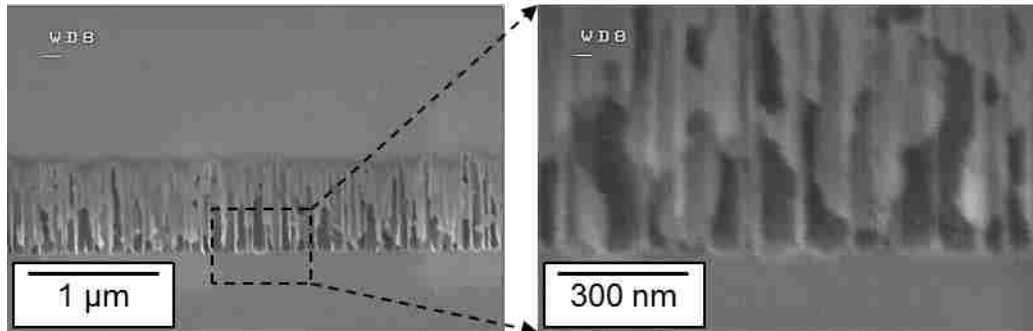


Fig. 3.3 The pores in the highly doped p-type silicon wafer have no branches and show concave interfaces form between the pore structures and the bulk silicon substrate.

3.1.2 Wet Etching

An anodization cell is designed for the electrochemical etching of a single crystal silicon shown in Fig. 3.4. The cell is mainly composed of three parts: an aluminum plate at the bottom as an anode, a Teflon block in the middle as an electrolyte container, and a platinum (Pt) wire at the

top as a cathode. The anode and cathode are connected to a power supply. In this experiment, a p-type silicon (Si) wafer is used for convenience compared to an n-type wafer in etching process for the following reason. In n-type Si wafer, the majority carriers are electrons, therefore it needs additional light illuminations in order to produce enough number of holes, because the etching process is active under the abundant holes. A highly doped p-type Si wafer, which has very low resistivity ($\sim 0.001 \Omega \cdot \text{cm}$), is placed on the aluminum plate and an aluminum foil is sandwiched in between the aluminum plate and Si wafer in order to improve the contact to the aluminum plate. Using aluminum foil makes the etching preparation much easier and faster instead of aluminum deposition on the backside of Si wafer. The etch area is defined by O-ring (25 mm in diameter) with a Teflon block on the Si wafer. The cell is tightened by 8 screws around the Teflon block and it is filled with a mixture of HF/ethanol having the volume ratio of 3:7. The applied current density is 13 mA/cm^2 through electrodes, and the processing time is 3 min.

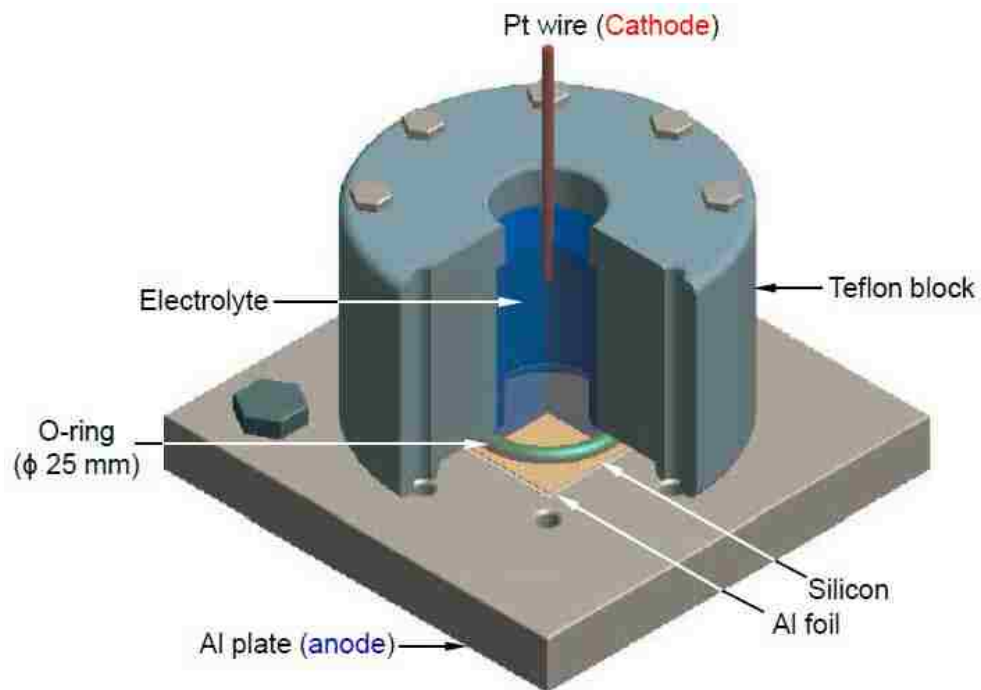


Fig. 3.4 Schematic of an anodization cell.

After the etching process, the PS is rinsed several times with ethanol and DI water and dried in ambient atmosphere. The PS periodically shows various colors from the center to the edge, where the color change is dependent upon the pore dimensions as shown in Fig. 3.5 (a) [72]. The reason for this difference in the pore dimensions is that the applied current from cathode to anode is not uniformly distributed with Pt wire under the HF/EtOH electrolyte. The outside of the colored circle in Fig. 3.5 (a) is the bare silicon, so the etched silicon wafer contains two different regions: the wet etched region and the bare silicon region. In this research, the target pore diameter is approximately 100 nm in order to use the structure as a master mold, however the SEM image in Fig. 3.5 (b) only shows smaller pores on the top of the PS.

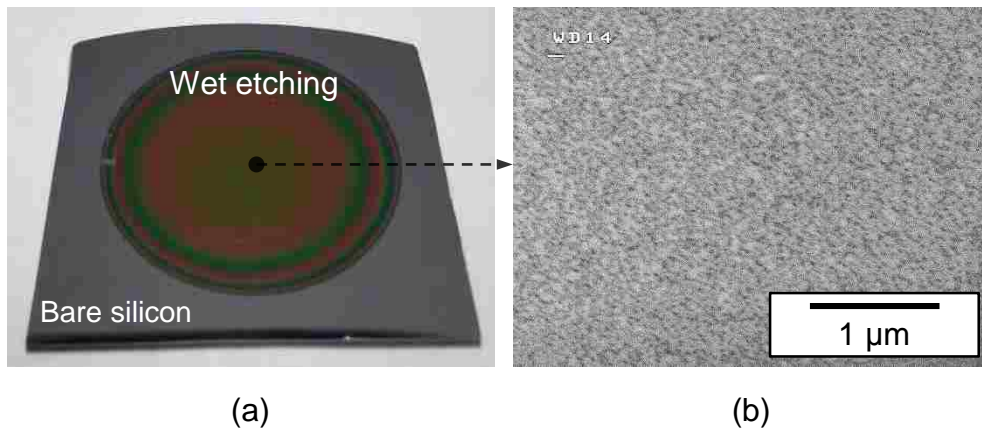


Fig. 3.5 Images of (a) electrochemically etched porous silicon and (b) SEM at the center of the sample.

3.1.3. Wet and Dry Etching

Dry etching of a porous silicon (PS) is followed after the wet etching process under a certain condition. The electrochemically etched PS is covered with micro pores on the top whose dimensions are even smaller than the inside of the pores at the deeper level. This is called a transition layer, which formation, the micro pores above the macro pores, is caused by the surface conditions of the silicon wafer, particularly the surface roughness [70]. In order to get a certain dimension of holes, the micro pores need to be slightly removed by reactive ion etching (RIE)

(PlasmalabSystem 100, Oxford Instruments.) Here, SF₆ is used as an etching gas and the applied flow rate is 40 sccm for 10 seconds with 200 W. The periodical color of the PS is changed after the RIE etching as shown in Fig. 3.6 (a). The SEM image in Fig. 3.6 (b) is also taken at the center of the PS, and it displays clear porosity in the SEM image compared with the PS before the dry etching. During the dry etching process, bare silicon regions, the outside of the PS boundary in Fig. 3.6 (a), are also exposed to the etching gas. The image also shows two different etched regions, the wet and dry etched region and the dry etched region only. Thus, the silicon wafer through the whole etching processes is divided into four parts: the bare silicon, the wet etched region, the dry etched region, and the wet and dry etched region.

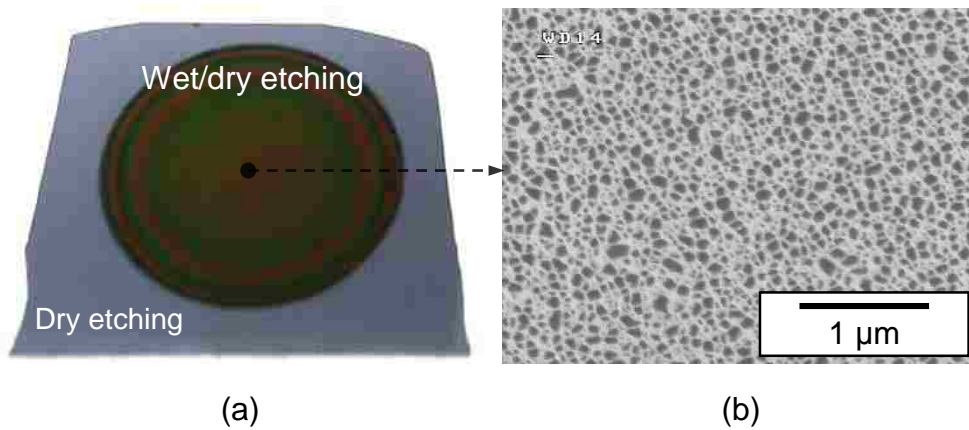


Fig. 3.6 Images contains (a) wet and dry etched porous silicon in the circle and also only dry etch silicon outside of circle, (b) SEM image at the center of wet and dry etched area.

For calculation of vertical dry etch rate, 45° angled SEM images are used. The cross sectional views of the schematic (top) and SEM (bottom) in Fig. 3.7 (a) show pore depths of about 1.24 μm only with the wet etching, but the removal of micro pores on the top changes the pore heights into approximately 990 nm through the dry etching as the schematic (top) and the SEM (bottom) shows in Fig. 3.7 (b). Thus, roughly 200 nm is etched for 10 seconds. This can be converted into 1.2 μm/min. This result is compared with normal silicon etching rate of 200 nm/min

under the same condition. Because of the high porosity, the etching rate of PS is 6 times higher than that of a bare silicon under the same etch conditions.

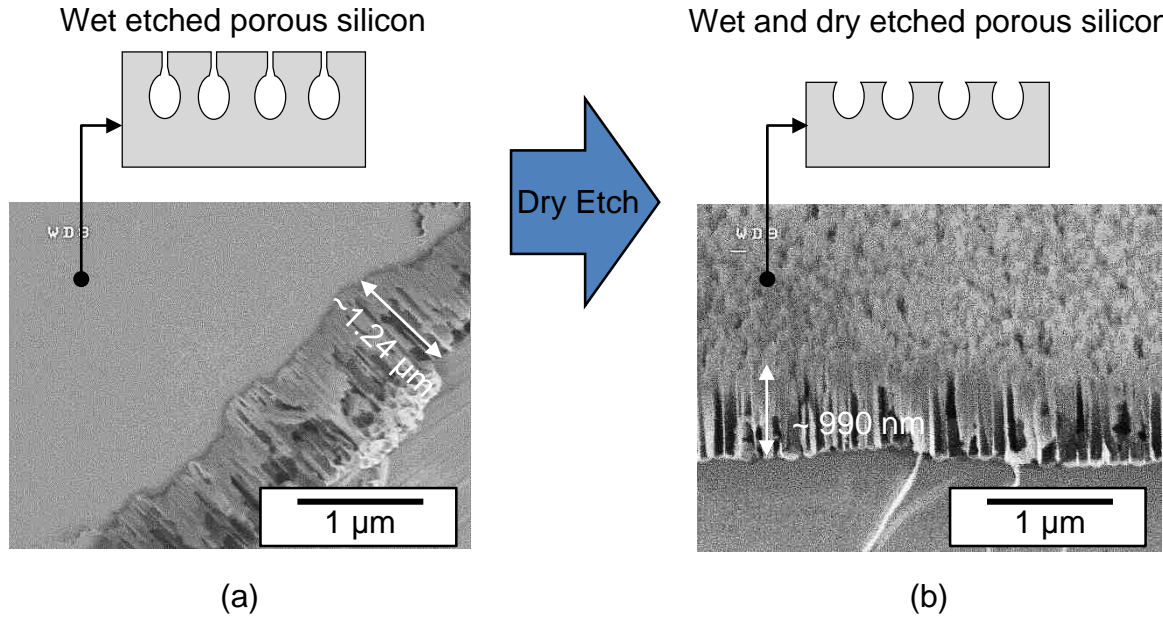


Fig. 3.7 The schematic comparison between (a) before and (b) after the dry etching with 45° angled SEM images.

3.2. Nanostructure Replication from Porous Silicon

In this study, porous silicon (PS) is used as a master mold in order to cast nanostructures from it. PS has a geometry that yields an extremely high surface-volume ratio, therefore direct replication is an issue for such a master mold. UV curable epoxy and PDMS are suitable candidates as a casting material. UV curable epoxy has a higher Young's modulus than PDMS, however its strong adhesion to silicon destroys the master mold when replicating. On the other hand, PDMS is able to easily cast from the master mold, because it is hydrophobic against silicon. However, the softness of PDMS causes tearing of cast films when it is peeled from the mold. Thus, in this research, a UV curable epoxy is chosen, and the disadvantage mentioned above is overcome by the following methods.

3.2.1. Gold Deposition as Releasing Layer

Anti-adhesion is one of the significant issues when feature dimensions are decreased to nano-scale because of the high surface-to-volume ratio [73]. Especially, in nanoimprint lithography (NIL), an anti-sticking layer decreases the stamp surface energy, and it is critical in protecting both the master mold and the imprinted features [74]. It is obvious that the anti-sticking agent has to cover the small structure as a thin, uniform, and conformal layer. In addition, the agent has to be inert and hydrophobic against the stamp material. Currently, it seems that silane has been widely used as an anti-sticking agent if silicon is used as a master mold. The chemical agent is preferred to be coated in a vapor phase rather than liquid phase, because vapor phase is able to coat uniformly to a small structure and also is not bothered by the wettability of the mold surface [75]. However, silane is a toxic chemical, and it needs a good ventilation system. In order to control the quality of anti-adhesion layer, a chemical vapor deposition (CVD) setup is required. Therefore, silane is not used in this research, however a gold (Au) coating can replace the role of silane. Gold naturally has a poor adhesion to Si. Au still shows similar characteristics to the porous silicon. A gold layer may be simply deposited by sputter or evaporator. Here, gold coating is performed by a sputter (Denton plasma coating) with the applied current 450 mA for 400 seconds. The thickness of the gold layer is basically controlled by the applied current and deposition time. The results show that gold thickness is approximately $20 \text{ nm} \pm 3 \text{ nm}$.

3.2.2. Epoxy Casting

Ultraviolet (UV) curable epoxy (Norland Optical Adhesive 68, Edmund Optics America) is a well-known material as an optical bond. The epoxy is only hardened when UV light is exposed for a certain amount of time. UV curable epoxy maintains its optical transparency before and after the curing, and it has a refractive index of about 1.54 which is very close to the refractive index of

glasses. A few drops of UV curable epoxy are gently placed over a thin gold (Au) layer on the wet and dry etched porous silicon (PS), and the liquid uniformly spreads and covers the substrate with a transparent plastic film. Under the 13 W UV light, the epoxy needed 5 minutes of hardening time, and it was easily peeled off from the PS because of the thin gold layer. The illustration in Fig. 3.8 (a) describes nanostructure casting procedure from PS. In addition, the images in Fig. 3.8 (b) show the cast UV curable epoxy from a quarter of the entire PS which thickness is about 500 μm . All releasing gold layers were transferred into UV curable epoxy with cast nanostructures which were necessary for Surface-Enhanced Raman (SER).

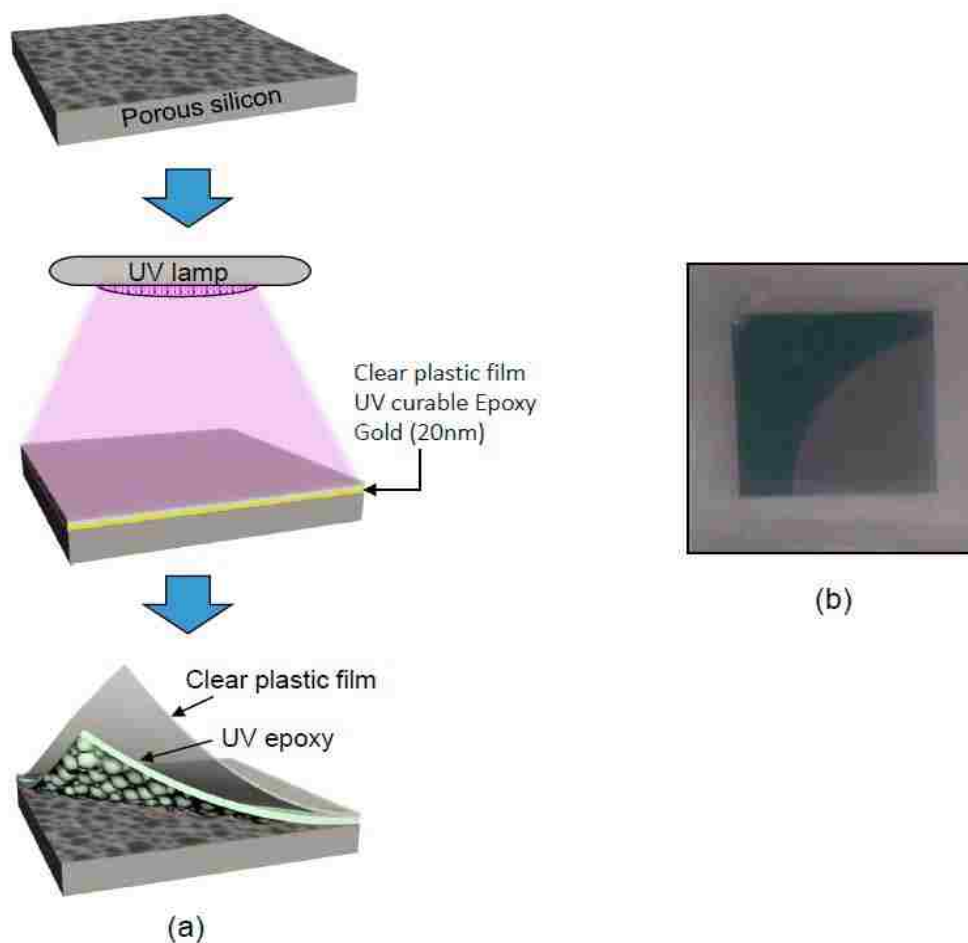


Fig. 3.8 (a) Illustration of nanostructure casting steps and (b) images of cast epoxy from porous silicon which has nanostructures inside of a quarter circle.

3.3. Measurement Setup of Surface-Enhanced Raman Scattering (SERS)

Raman spectra are measured with Raman spectroscopy which basically detects inelastic scattering with monochromatic light, and the spectroscopy is able to measure many molecules in different phases including solid, liquid, and gas. The spectroscopy is composed of four parts: a light source, a light illumination and collection system, a wavelength selector, and a detector. In this research, a Raman spectrometer (LabRAM, HORIBA JOBIN YVON) utilizes a 1 mW 633 nm wavelength laser with a long working distance 50x (N.A. = 0.55) objective purchased from the Olympus Corporation. In general, there are three types of SERS measurement using conventional Raman spectroscopy, namely, target molecule drop and dry on the SERS active area, target molecule flowing with SERS active nanometallic particles, and target molecule flowing over SERS active area as illustrated in Fig. 3.9 (a), (b), and (c), respectively. The first method, drop and dry in Fig. 3.9 (a), presents the highest Raman signals, because the target molecules are concentrated and are strongly bonded to the metal feature as the solvent dries out. The second method, flowing target molecule with SERS active nanometal in Fig. 3.9 (b) does not show as high Raman intensity as the first method, because less quantity of the target molecules are involved in SERS. Moreover, the third method, target molecule flowing over the SERS active area in Fig. 3.9 (c) also shows weak Raman signal compared to the first method, since the target molecule freely moves in a fluidic channel and only a few molecules diffused into the SERS active area contribute to the enhancement. In comparison with SERS measurement methods in drop and dry as Fig. 3.9 (a) and liquid as Fig. 3.9 (b) and (c), SERS enhancement with liquid are relatively less intensive.

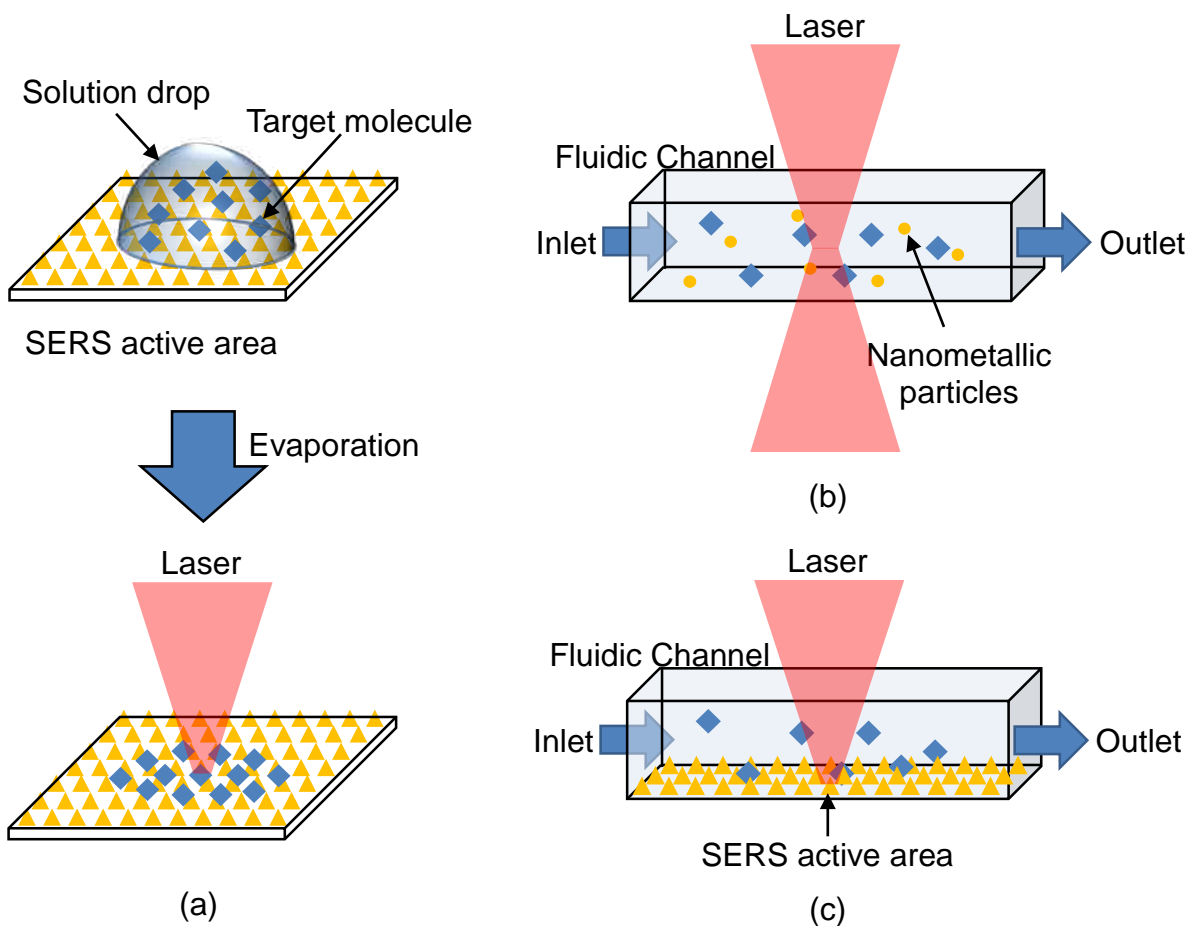


Fig. 3.9 Typical Surface-Enhanced Raman Scattering (SERS) measurement methods including (a) drop and dry, (b) flowing target molecule with SERS active nanometallic particles, and (c) target molecule flowing over SERS active area. After reference [76]

In this research, target molecules are detected over a nanometallic surface with liquid, since this measurement is closer to a real detection method with an endoscope under critical condition. In order to make a reliable measurement setup, fluidic cell is built with glass slides, metal tube with 1 mm outer diameter, and coverslip at the top as shown in Fig. 3.10 (a). Glass body is preferred to polymer such as PDMS or PMMA because glass has less back ground Raman spectrum and its transparency is better than any other material. Glass also does not need additional fabrication step except for the assembly. Each part is bonded by a transparent resin. The fluidic cell is attached to the wooden block which is designed for measuring the reflection and transmission of the fluidic

cell with stability, because the fluidic cell is not geometrically stable by itself when it is loaded onto the Raman stage. The measurement schematic is illustrated in Fig. 3.10 (b). An analyte is injected by syringe into the inlet and it is held during Raman measurement. After the measurement is completed, the analyte is drained through the outlet. Fig. 3.10 (c) describes each layer of the active area including the cast nanorough gold on epoxy.

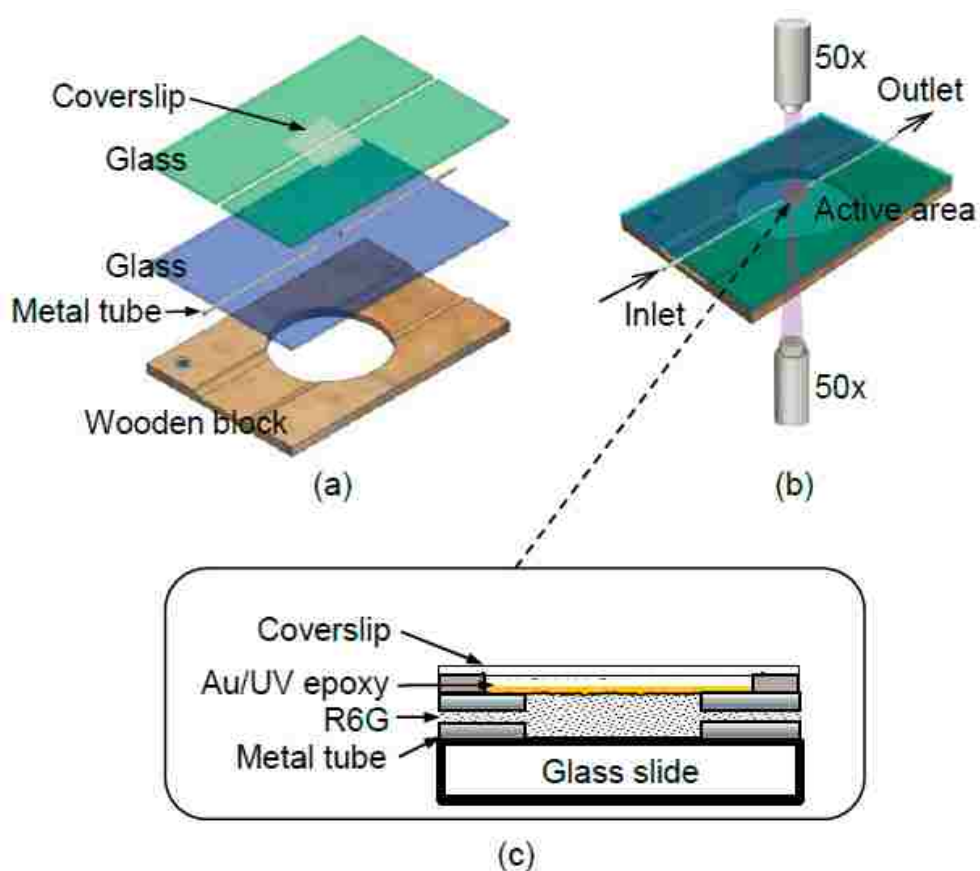


Fig. 3.10 The schematic of (a) fluidic cell parts including different sized glass slides, metal tube with 1 mm outer diameter, and wooden block, (b) a direction of injecting target analyte into the fluidic cell, and (c) zoomed active area having several layers containing nanorough gold on epoxy.

CHAPTER 4. TRANSPARENT SURFACE-ENHANCED RAMAN SCATTERING SUBSTRATE CHARACTERIZATION

In this chapter, the nanorough gold on epoxy needs to be optimized for on the gold thickness. Optimized gold thickness can provide maximum SERS enhancement and can help build a suitable endoscope probe. In order to analyze SERS spectrum, all background spectra must be measured. Some target analytes have to be prepared with different concentrations to observe detectable ranges. At the end of this chapter, the actual measured spectra in reflection and transmission are provided, and their values are also compared to select the optimal condition of the nanorough gold on epoxy.

4.1 Different Gold Thickness Deposition

Surface-Enhanced Raman Scattering (SERS) is dependent upon shapes, sizes, and distances between nanostructures. In this research, forms of nanostructures are initially determined by a pore shape of the porous silicon (PS) as a master mold. After the nano-features are cast, the size and the distance between the nanostructures can be modified by metal deposition. Here, different gold (Au) thicknesses are deposited over the cast rough epoxy from the PS. The same sputtering machine is used when Au releasing layer is deposited. When the epoxy is cast from the PS with the releasing layer, non-continuous Au releasing layers are transferred to the epoxy, because of the epoxy adhesion to gold layer. On top of the non-continuous Au layer, additional Au layers are sputtered with thicknesses of 20 nm, 50 nm, and 80 nm shown in Fig. 4.1 to find an optimal Au thickness for the transparent SERS substrate.

When wet etched silicon went through a dry etching process, two kinds of etching regions, the wet and dry etched and only the dry etched area, were eventually formed as explained in subchapter 3.1.2. The wet and dry etched and only the dry etched areas were cast at the same time. As a result, the cast UV curable epoxy contained both regions on the same sample: the dark color




Additional gold thickness	20 [nm]	50 [nm]	80 [nm]
Cast epoxy			

Fig. 4.1 Different additional gold thicknesses (20 nm, 50 nm, and 80 nm) on cast epoxy from wet and dry etched silicon.

is the additional gold on wet and dry etched area and bright yellow color is the additional gold on only the dry etched areas. When gold is covered on both areas, the surface morphologies show different patterns. The SEM images in Fig. 4.2 (a) and (b) show 60 nm of gold deposition on the cast epoxy substrates with only the dry etched area and with both wet and dry etched area, respectively. The gold on the cast epoxy from wet and dry etched area in Fig 4.2 (b) has more roughness than the one on the cast epoxy from only dry etched area in Fig 4.2 (a). The different roughness is able to contribute to different enhancements of SERS.

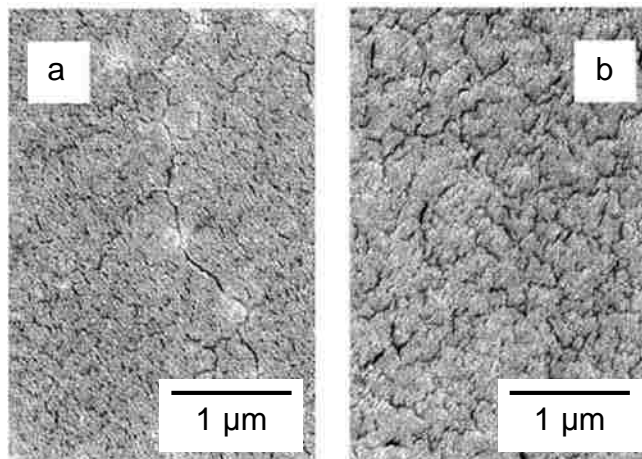


Fig. 4.2 UV curable epoxy is cast from (a) dry etched area and (b) both wet and dry etched area, and 60 nm of gold is deposited on (a) and (b) [77].

However, SEM images are not sufficient to provide quantitative number of roughness to such small surface morphologies, therefore the images of atomic force microscopy (AFM) are taken to see the surface roughness in Fig.4.3. AFM images of the two cast epoxy substrates, the

wet and dry etched and only the dry etched areas are shown in Fig. 4.3 (a) and (b), respectively, where each substrate is covered with 40 nm of gold. Root mean square (RMS) height variation of both prepared epoxy samples are measured by AFM. A cast epoxy from only the dry etched area with the gold deposition shows relatively smooth surface morphology in Fig. 4.3 (a) and its RMS height variation is 14 nm. On the other hand, the epoxy from the wet and dry etched area with the same amount of gold thickness shows a rougher profile in Fig. 4.3 (b), and the RMS height variation measured is 32 nm. These RMS height variations are quite comparable to the AFM images.

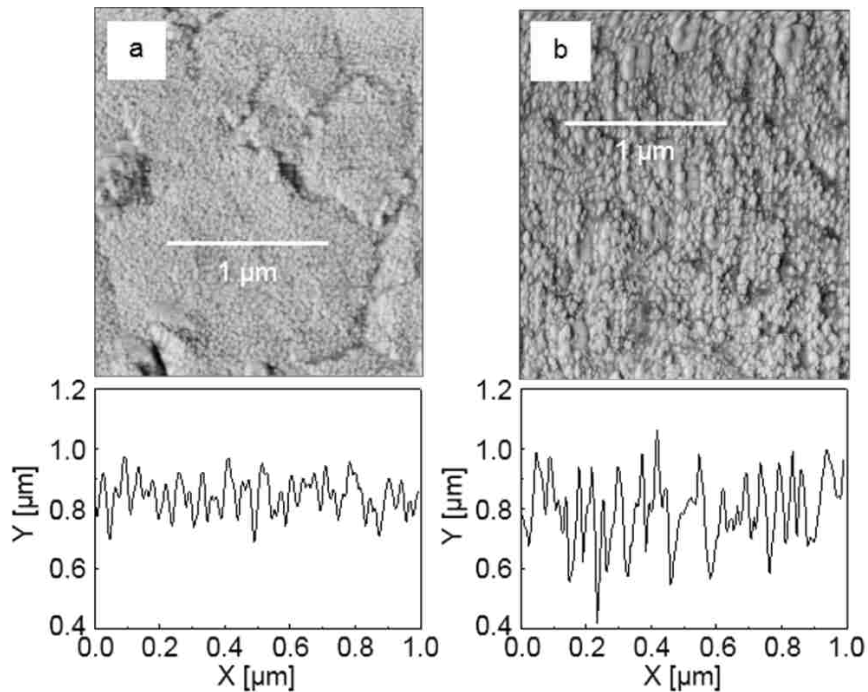


Fig. 4.3 AFM images of 40 nm gold on epoxy substrates casting from (a) only dry etched region and (b) both wet and dry etched region. The roughness of two regions are compared within the scanned 1 μm range. The RMS roughness is 14 nm on only the dry etched region and 32 nm on the both wet and dry etched region. [77].

4.2 Background Raman Signals

A fluidic cell as described in the previous section was developed for Surface-Enhanced Raman Scattering (SERS) measurement. The detection areas of the fluidic cell are composed of

layers including two microscope slides, a thin gold layer bonded to epoxy, and coverslip. All of these substances are optically transparent, so when laser beam is focused on the SERS activation site of the fluidic cell, different Raman signals can be observed at the focused target. In addition, Raman spectra of gold coated epoxy cast from the two etching methods, namely the dry etching only and a combination of the wet and dry etching, are compared when air and DI water flow through the fluidic cell as shown in Fig. 4.4, because some target solutions are almost transparent at low concentrations, and therefore the background Raman signals can help clarify the identification of the target solution.

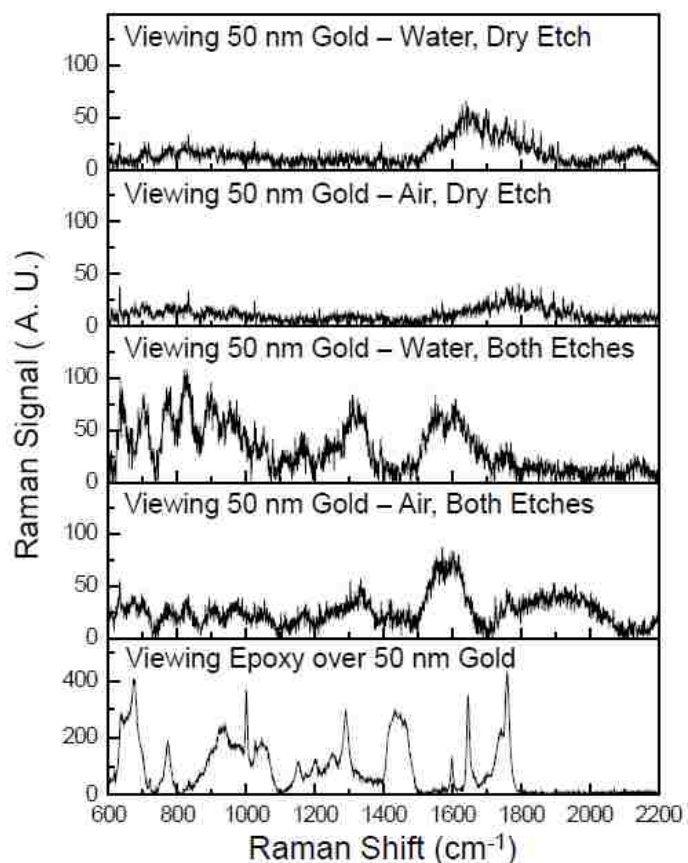


Fig. 4.4 All background spectra involved in the fluidic cell development. Particularly, epoxy shows the highest spectrum, but the overall peaks are not overlapped with the peak of a target molecule, Rhodamine 6G [77].

4.3 Target Material Preparation

4.3.1 Rhodamine 6G (R6G)

Rhodamine 6G (R6G) organic dye is widely used in biological applications including flow cytometry [78, 79], fluorescence correlation spectroscopy [80, 81], fluorescence microscopy [82, 83] and enzyme-linked immune sorbent assay (ELISA) [84], because of its easy detection and chemical stability. R6G is widely used for SERS analysis because it has a large cross-sectional Raman scattering [85]. The chemical formula of R6G is $C_{28}H_{31}N_2O_3Cl$ as shown in Fig. 4.5 and its molecular weight and solubility in 25 °C water are 479.01 g/mole and 20 g/L, respectively [44].

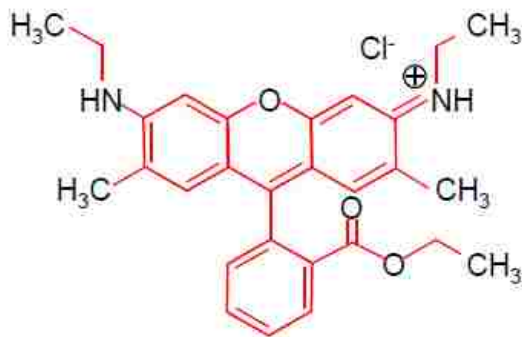


Fig. 4.5 Chemical structure of Rhodamine 6G.

For SERS detection through the nanorough gold in a fluidic cell, R6G powder was dissolved in water at room temperature, and R6G solutions were prepared in different concentrations from 1 mM to 1 nM. The solutions are visibly red at higher concentrations, but when it is diluted below 1 μ M, the color becomes almost transparent (Fig. 4.6).

4.3.2 Gelatin with Rhodamine 6G (R6G)

A transparent Surface-Enhanced Raman Scattering (SERS) substrate was developed to support early detection of abnormal tissues in medical diagnosis. Rhodamine 6G (R6G) solutions were a good analyte for a prototype *in-vitro* measurement of the transparent nanorough gold, but R6G solution dissolved in water was not similar to biological environment such as a human tissue.



Fig. 4.6 Different concentrations of Rhodamine 6G solutions.

Therefore, gelatin was used in order to prepare an artificial condition like a human tissue [86]. Gelatin is basically composed of peptides and proteins derived from tendons, ligaments, skins, corneas, and guts. It was easily mixed with hot water and it became a transparent gel during cooling. The mechanical properties of the gel depended on the concentration of gelatin in water.

A gelatin (Knox unflavored gelatin, Kraft Foods Global, Inc.) was mixed with R6G solution. Gelatin was prepared according to the instruction that provided by the product. However an R6G solution in DI water was used instead of drinking water as a solvent. 5 ml of R6G solution with different concentrations were heated to 50 ~ 60 °C, and 1 g of gelatin powder was dissolved



Fig. 4.7 Gelatin with different concentrations of Rhodamine 6G.

into the warm R6G solution. In order to facilitate the mixing, it was stirred until gelatin particles are not visible, and then the mixture was left at room temperature for 2 hours. Fig. 4.7 shows the final form of gelatin with R6G analytes.

4.4 Reflection and Transmission of Nanorough Gold in Fluidic Cell

A transparent Surface-Enhanced Raman Scattering (SERS) substrate, called nanorough gold, was prepared with gold (Au) deposited on cast epoxy from the porous silicon (PS). For the SERS enhancement, the transparent SERS substrate was tested under a Raman spectrometer with Rhodamine 6G (R6G) solution. As stated in the previous chapter, the R6G solutions were injected through a fluidic cell which was assembled with a transparent nanorough gold substrate. The fluidic cell was measured on the Raman specimen stage, and a laser beam was directly focused on the top of the nanorough gold, called “viewing gold” equal to reflection measurement. Different concentrations of the analytes, a factor of 10^6 from 1 nM to 1 mM of R6G, were injected through a fluidic channel having 1 mm² in cross-sectional area. Solutions with a lower concentration were first injected in order to minimize the interaction with higher concentrated solutions. The laser was focused on the nanorough gold with 80 nm gold deposition through the glass-slide, on the bottom layer of the fluidic cell. The measured results are shown in Fig. 4.8 with different concentrations of analytes over the surface of the nanorough gold substrate. One assumption in this measurement is that no concentration change occurs when a higher concentrated solution replaces a lower concentrated solution. The original 50x objective on the spectrometer has a short working distance, so it does not provide an appropriate moving range for a multi layered fluidic cell. Therefore, the objective was replaced with a compatible long working distance 50x objective (ULWD MSPlan 50, Olympus Co. of the America) for all measurements.

According to the etching process, three different substrates including the not etched, only the dry etched, and the wet and dry etched silicon are prepared. SERS measurements of these three substrates with 80 nm gold deposition were carried out, and different concentrations of R6G from

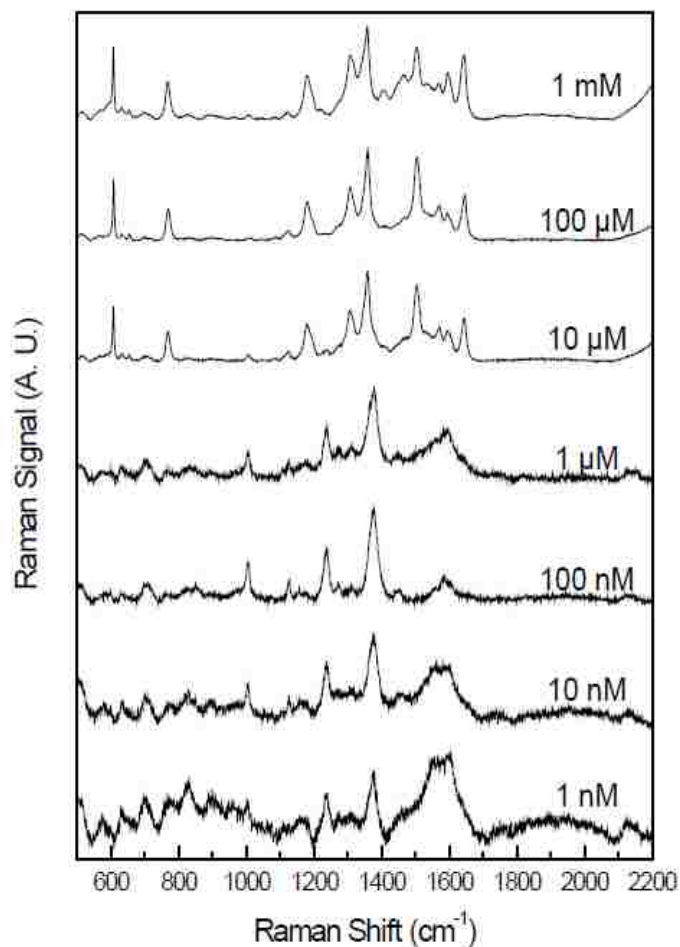


Fig. 4.8 Raman signals from 80 nm of gold in contact with the Rhodamine 6G solutions with concentrations ranging from 1mM to 1 nM [77].

1 nM to 1 mM were applied. The strongest signal was measured for the cast epoxy from the both wet and dry etched silicon in the applied R6G concentrations as shown in Fig. 4.9.

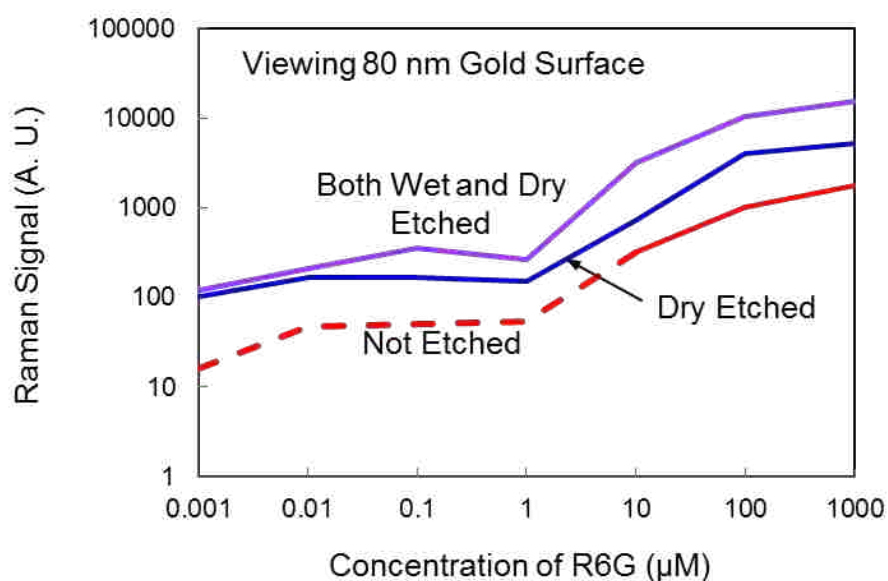


Fig. 4.9 Raman signals from 1 nM to 1 mM R6G on 80 nm gold on three types of substrates. The intensities of the Raman signals was obtained at the 1362 cm^{-1} and signals from both etches shows the highest signals. The dotted curve shows shifted peaks in spectrum below $1\text{ }\mu\text{M}$ R6G solution on the substrate with no etch [77].

The cast epoxy from the unetched silicon shows the lowest signal compared to the other two etching methods for all concentrations. Fig. 4.10 shows the measured R6G spectra of the cast epoxy substrate with 80 nm gold deposition. Overall, the spectra show a similar shape for all types of the cast epoxy substrate with different etching processes in the scanned range. However, below $1\text{ }\mu\text{M}$ of R6G, the spectrum is slightly shifted. It is believed that it still belongs to the R6G spectrum because the reference peak remains the same at around 1362 cm^{-1} .

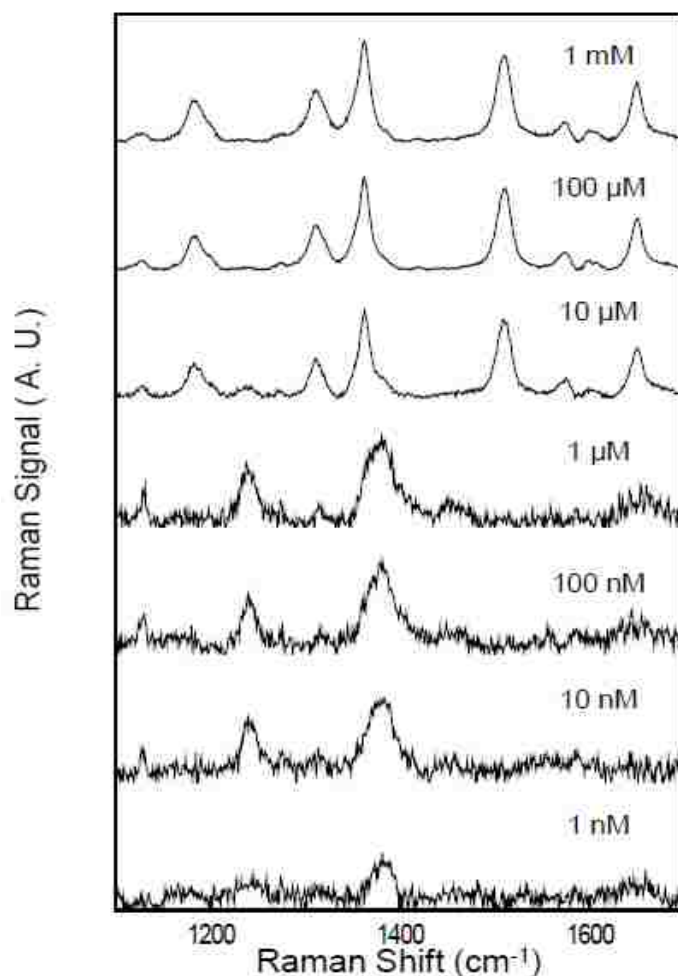


Fig. 4.10 Surface-Enhanced Raman spectra on the cast epoxy substrate with no etching of the silicon wafer [77].

SERS measurements in reflection and transmission were also compared with different gold thicknesses. In contrast to the reflection measurement, transmission measurement means laser beam is focused on the nanorough gold after passing through glass and epoxy. Firstly, reflection measurement of both wet and dry etched and only dry etched silicon wafers was analyzed. The applied gold thicknesses are 20 nm, 50 nm, and 80 nm over the cast epoxy, and the R6G spectra of are measured ranging from 1 nM to 1 mM within the fluidic cell, and the results are compared with the reference spectrum of 1362 cm^{-1} in Fig. 4.11.

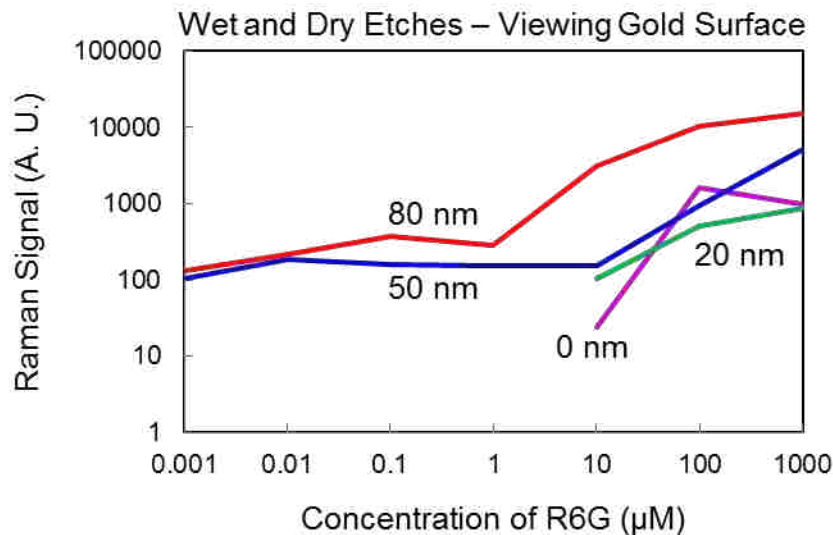


Fig. 4.11. Surface-Enhanced Raman signals with additional gold on the epoxy casting from both wet and dry etched silicon wafer. The cast substrates with 20 nm gold and no additional gold can only detect R6G signals above the concentration of 10 µM. [77].

The epoxy casting from the wet and dry etched silicon is comparable to the epoxy casting from only the dry etched silicon. The Raman signal intensity of R6G over the epoxy casting from only the dry etched silicon was also measured with different concentrations shown as Fig. 4.11. The overall Raman intensities of cast epoxy from only dry etched silicon are lower than the cast epoxy from the both wet and dry etched silicon. In addition, it was observed that the pattern of the signal intensities by concentrations in Fig. 4.12 are quite similar to the ones in Fig. 4.11. Gold was sputtered under the same processing conditions, and the difference in Raman intensity between the two substrates shows the effect of the wet etching such as porous structures. In this measurement using cast epoxy from the dry etched only silicon, the Raman intensities could not be measured for concentrations below 1 µM of R6G for samples with 0 nm and 20 nm of additional gold deposition.

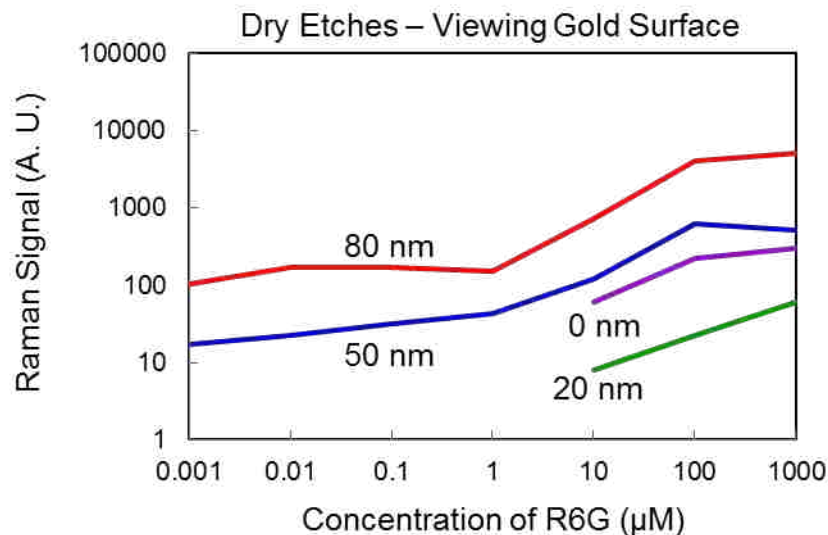


Fig. 4.12 Surface-Enhanced Raman signals with additional gold on the epoxy casting from dry etched only silicon wafer. The cast substrates with 20 nm gold and no additional gold can only detect R6G signals above the concentration of 10 µM.

Transmission measurements of the cast epoxy substrate with gold deposition were different from the reflection measurements. A fluidic cell containing the epoxy substrate was flipped, so that the gold layer on a cast epoxy was facing down against the incident laser beam, called “viewing through gold.” The transmission of the SERS measurement can be achieved, because the cast epoxy substrate with thin gold deposition is optically transparent as seen in subchapter 4.1. For transmission measurements, analytes ranging from 1 nM to 1 mM of R6G were injected by a syringe to fluidic cell as reflection measurement, and the same gold thicknesses 20 nm, 50 nm, and 80 nm were employed. All results were compared as shown in Fig. 4.13 with the reference spectrum of 1362 cm⁻¹. In low concentrations below 1 µM, the measurement SERS signals could not be obtained. The transmission characterization is important for building an endoscopic probe, because an optimum gold thickness needs to be determined for the highest sensing performance.

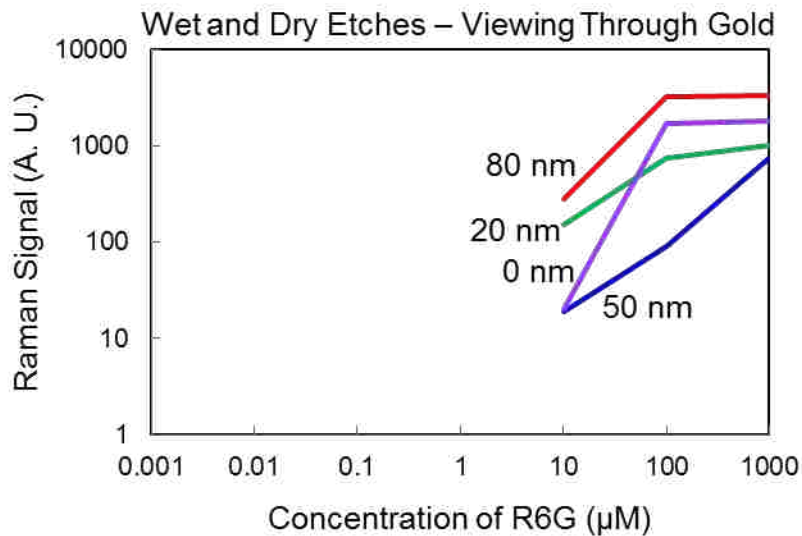


Fig. 4.13 Transmission of Surface-Enhanced Raman signals from epoxy casting from both wet and dry etched silicon with different gold thicknesses [77].

The transmission measurement of the cast epoxy from only the dry etched silicon was also performed. The R6G signals from the measurement was detected only ranging from 10 μM to 1 mM, but the measurement graph in Fig. 4.14 does not show any trend comparable to that of the cast epoxy from the both wet and dry etched silicon. The cast epoxy with no additional gold shows the highest R6G signal in the measured range. As a gold layer was added with 20 nm, 50 nm, and 80 nm thicknesses, it is difficult to see any trend especially for the 20 nm additional gold deposited epoxy.

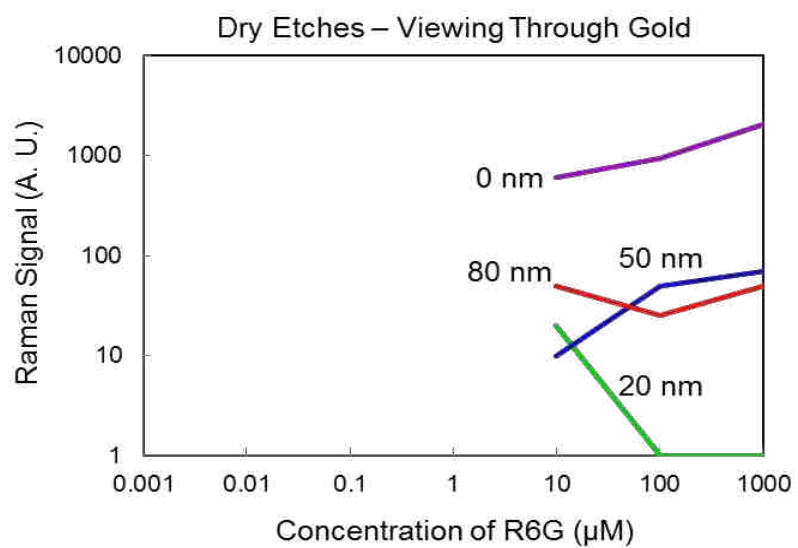


Fig. 4.14 Transmission of Surface-Enhanced Raman signals from epoxy casting from only dry etched silicon with different gold thicknesses.

CHAPTER 5. REMOTE RAMAN

In this chapter, a remote Raman apparatus was built with a transparent Surface-Enhanced Raman Scattering (SERS) substrate as described in the previous chapters. In principle, the apparatus is composed of two parts: light transmission instrument and probe head. The light transmission instrument consists of multiple mirrors, arms and joints, which is called an articulated arm. The probe head contains a transparent SERS substrate, a gradient-index (GRIN) lens (NSG Group) and a small positive lens. Eventually, the collected SERS signals from the probe head are transmitted to a spectrometer through the articulated arm for analysis.

5.1 Photon Transmission

In this research, a single mode fiber was tested with the GRIN lens for light guides, however strong background signals of the silica-glass fiber blocked the Raman signal from the target. In order to overcome the drawback, many research groups have used two optical fibers; one for the excitation light transmission and the other for the scattered Raman signal collection [87-89], but this method increases the total volume of the probe as a result of the complex geometrical designs. In addition, some research groups have successfully collected Raman signals through a single optical fiber with high power of the incident laser [90] and a hollow optical fiber [91]. However, the replacement of the laser is accompanied with sample damages and increased costs for the equipment. Some hollow photonic-crystal fibers were commercially available, however it does not provide high numerical aperture (NA) and transmission wavelengths of the fiber are limited during this research.

As an alternative method, external light transmission instrument, which is called an articulated arm, is built with several mirrors, arms and rotating joints as shown in Fig. 5.1. The light guided with the articulated arm is able to travel to remote sites as long as the arm can approach

the target. After taking microscope objective away from the spectrometer, the laser beam is slightly diverging, so an additional single positive lens which has a long focal length is placed in between M_1 and M_2 . Thus, the laser beam is focused to a waist at the image distance of the lens, and the beam starts to diverge, again. When the beam reaches GRIN lens surface, the spot diameter is the same as GRIN lens diameters. Then, the laser beam is focused on the nanorough gold through GRIN lens.

The total number of the applied mirrors in the light transmission instrument is seven: two external mirrors guiding the light to the articulated arm and five internal mirrors in the articulated arm. M_1 on the stage of the spectrometer directs the incident light to the arm entrance and M_2 on the base of the arm support directs the light along the axis of the arm. The combination of the M_1 and M_2 mirrors is able to precisely manipulate laser beam paths: M_1 for laser beam positions and M_2 for laser beam angles. The incident light can also be rotated with the right angled elbows where 45° tilted mirrors are mounted, and the rest of the mirrors at elbows are united with arms. B is located on a circle of radius L_1 (34 cm) length on point A, and point C makes another rotation of a radius L_2 by the centered point B based on the illustration in Fig 5.1. A couple of mirrors at the last two rotating joints enable the laser beam to point at any direction. Therefore, the probe head can be positioned within the toroidal volume that is scanned by the circular rotations of the two arms. The practical scanning volume is about 1/6 volume of torus which is determined by the lengths of two arms. In this design, L_1 is basically longer than L_2 , therefore it is able to scan the volume of $2\pi L_1 \times (\pi L_2)^2$. Since the articulated arm is placed on a support table, the motion range of the arm (L_1) is limited to 90 degrees. The power loss of laser beam at each reflection of the mirrors in rotating joints is about 10.2% and total transmission is about 58%.

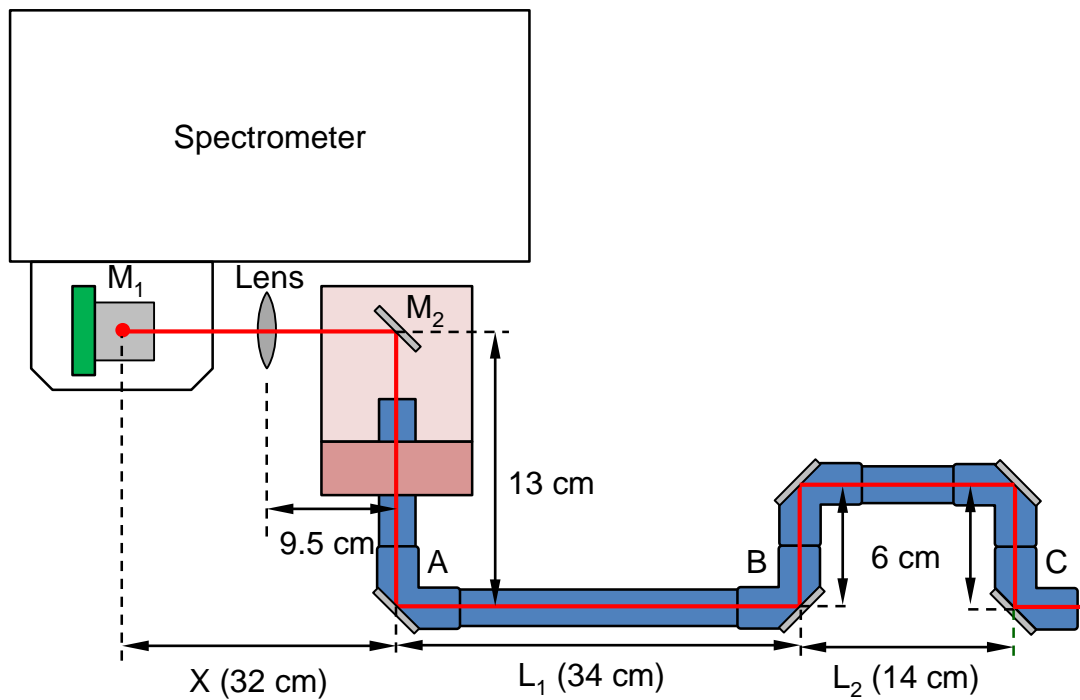


Fig. 5.1 The schematic of the remote Raman apparatus with the top view.

5.2 Probe Head Design

The probe head is one of the most significant parts in a remote Raman apparatus because the probe head needs to contact the target analytes during a scan. Thus, the probe head must be small both and biocompatible. The probe head mainly consists of two elements: a GRIN lens and a SERS substrate. A GRIN lens is designed to focus the light using a continuously changing refractive index as shown in Fig. 5.2. The light within the lens material follows a sinusoidal path, therefore a full length of the light path is 2π which is known as one pitch. GRIN lenses are available with diameters of 1 and 2 mm. Also, GRIN lenses are available that focus the light on the back surface of the lens, so it allows for a direct contact with the target specimen. Because of their small diameter GRIN lenses are often used in optical probes. In this probe head development, two types of cylindrical GRIN lens, 2 mm in diameter and 2.6 mm and 5.2 mm in length, were tested. The periods of the GRIN lens correspond to $\pi/4$ and $\pi/2$, respectively as illustrated in Fig. 5.2 (a) and (b). If parallel light enters a $\pi/4$ GRIN lens, the light is focused at a point with a significant working distance. If parallel light enters a GRIN lens with a $\pi/2$ period, the light is focused at the other end of the GRIN lens.

Instead of direct attachment of SERS substrates to the GRIN lens, a first design was proposed for test purposes of GRIN lens with SERS substrate on glass slides. Thus, the SERS substrate was initially bonded to the glass slide with ultraviolet (UV) curable epoxy which has the same refractive index as glass. The nanorough gold (Au) of the SERS substrate was attached to the target area at which an incident parallel beam from the spectrometer was focused through the GRIN lens, air gap, and a layer of the epoxy. The GRIN lens, 2 mm in diameter and 2.6 mm in length, had a period of $\pi/4$, and it was implanted in a screw which has a hole 2 mm in diameter

(Fig. 5.3). Focus of the light on the nanorough gold of the SERS substrate was manipulated by adjusting the height difference of the GIRN lens along the screw.

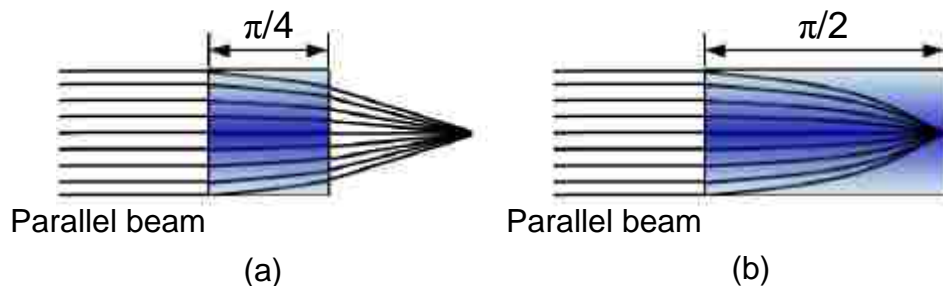


Fig. 5.2 The schematic of light propagation in (a) $\pi/4$ and (b) $\pi/2$ gradient-index (GRIN) lenses.

Through the articulated arm, the Raman spectrum measurement was tested with 1 mM Rhodamine 6G (R6G). 5 ml of 1 mM R6G solution was mixed with 1 g of the gelatin powder to form a gel. The first probe head was moved and gently pressed into the gel to make a proper contact with the nanorough gold surface. The screw with GRIN lens was positioned through the threads in order to make a focus. In about 1 mm distance away from the lowest position of the screw, the first type of probe gathered R6G signals, but the intensity was relatively low as shown in Fig. 5.4.

It is believed that the low Raman intensities are related to the issues of inaccurate focusing with the inserted $\pi/4$ GRIN lens in the screw, and the additional gaps associated with air and glass between the GRIN lens and the SERS substrate. In the probe head, the GRIN lens is placed in the short screw which has a wide pitch and is wiggled with the thread, and therefore there are some difficulties for precise focuses. This indicates that the GRIN lens cannot focus the laser beam properly at the right position of the nanorough gold. In addition to the focusing, the laser beam from spectrometer causes light intensity loss due to beam spots larger than the diameter of the GRIN lens. In order to build an improved probe design, it was decided to add one more single

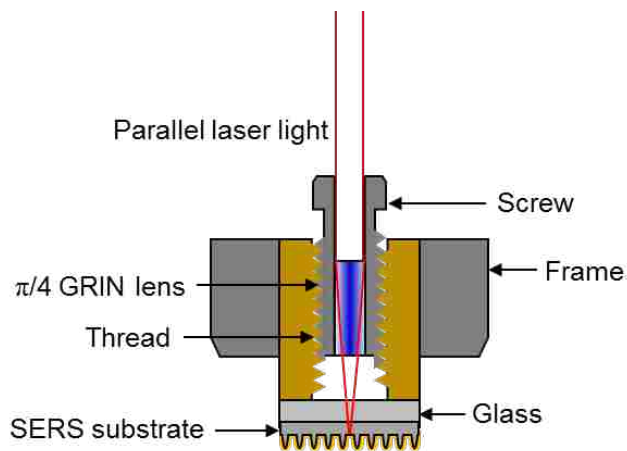


Fig. 5.3 The first probe head is assembled with the GRIN lens and the SERS substrate in the housing. The GRIN lens is positioned with the screw and the SERS substrate is attached to the glass for the first design.

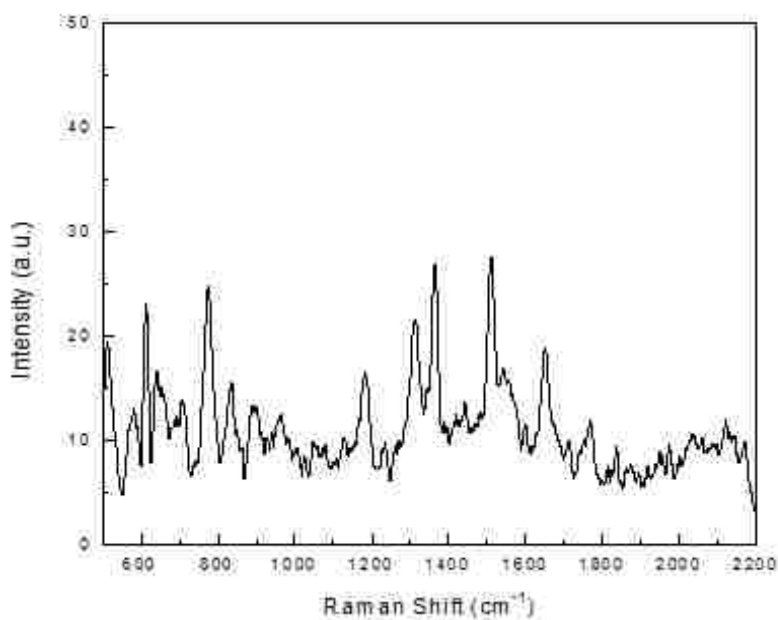


Fig. 5.4 The remote Raman spectrum of the mixture (5 ml of 1 mM of Rhodamine 6G and 1 g of the gelatin) is measured under the initial remote Raman apparatus.

positive lens right before the GRIN lens. The second positive lens is able to make the slightly diverging beam into a converging beam in the space between the lens and the GRIN lens, and it diverges again toward the surface of the GRIN lens. The incident angle of laser beam from the second external positive lens to the GRIN lens determines the ultimate focusing distances after the GRIN lens. Moreover, $\pi/2$ GRIN lens with the second external positive lens provides a much higher axial magnification than the $\pi/4$ GRIN lens with a parallel laser beam. This helps to obtain a focus. In the experimental setup shown in Fig. 5.5, a suitable distance between the single positive lens and the GRIN lens must be found in order to make the accurate focus on the gold surface. In addition, the schematic at the bottom of Fig. 5.5 describes how the laser light propagates from the second positive lens to the GRIN lens, and it also shows the specific dimensions and distances of all lenses. If it is well focused on the nanorough gold surface through the GRIN lens, the same laser light in size and path is reflected back to its original location. Then, the distance between the external positive lens and the GRIN lens was found for the probe head design. In the optical benchtop setup, a He-Ne laser is directed to the positive lens, 7.5 mm in diameter, through a 2 mm aperture in diameter. The focal length of the lens is 17.8 mm, and the initial distance between the second lens and the GRIN lens is 31.5 mm. The GRIN lens is placed on the x-y micrometer stage, so the GRIN lens position is moved to the positive x direction with a step of 254 μm . In order to make the reflection of the laser beam through the GRIN lens, 20 nm thickness of gold is deposited on a 250 μm thickness of smooth epoxy, and the nanorough gold substrate is attached to the GRIN lens with the UV epoxy. Thus, the total thickness of the epoxy is approximately 400 μm .

A series of images are taken from the location of the 2 mm aperture by moving the GRIN lens in the x direction, and the photographs on the left side of Fig. 5.6 show the reflected laser on the aperture. The illustrations describe the laser beam path before and after the GRIN lens. As

mentioned earlier, the GRIN lens moves away with a step of 254 μm , but only eight pictures are chosen from the sequential pictures. When a distance of GRIN lens is 35.31 mm apart from the send lens, the laser beam is focused on 20 nm gold layer on epoxy which thickness is about 380 μm . At this distance, the size of the laser beam just fills GRIN lens. If the GRIN lens moves closer to or further away from 35.31 mm, the laser beam through the GRIN lens becomes out of focus at the gold layer.

An improved probe head was designed based on the lens focusing measurements. A block of aluminum was machined for the rigid housing and a 3 cm stainless steel tube was assembled by a thread for probe tip. A small positive lens was implanted in the housing, and $\pi/2$ GRIN lens (2 mm in diameter and 5.2 mm in length) was inserted at the end of the tube with nanorough gold.

In Fig. 5.7 (a), a photograph of the improved probe is displayed with the names of each element. The probe was installed in the articulated arm. Depending on the movement of the GRIN lens in the probe tip, the focusing position is changed. Figure 5.7 (b) displays the photographs taken from the computer monitor of the Raman spectrometer, and they show the focused spots at the various distances away from the closest points to the second external positive lens. One turn of the thread equals to about 0.790 mm in displacement. According to the pictures, the smallest laser spot is achieved when the thread is rotated 6.5 turns which corresponds to about 5.135 mm, but the focused spot position is slightly changed due to the thickness of the cast UV epoxy ranging from 300 μm to 500 μm . The variation is offset by the movement of the probe tip with GRIN lens.

Locations of the focused laser on the nanorough gold through air, GRIN lens, and UV curable epoxy are experimentally verified by visual changes on the monitor of spectrometer. In addition to the experimental measurements, the focusing distances of the illuminated laser through

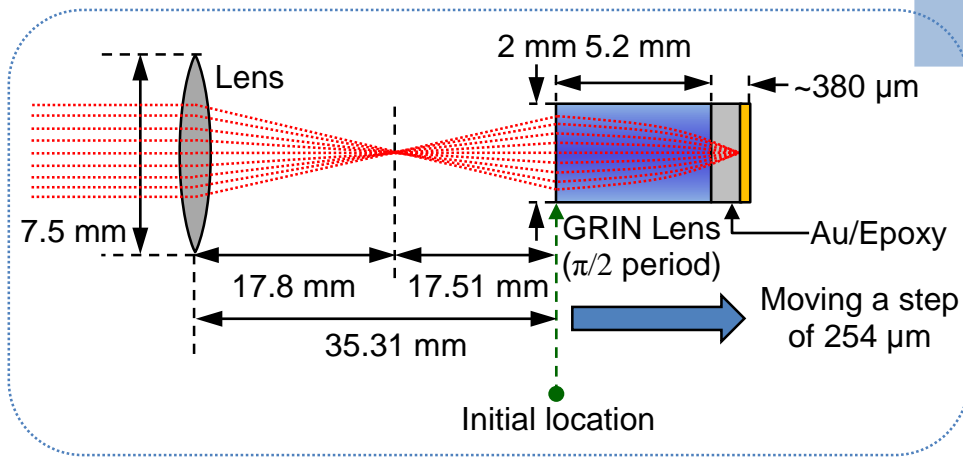
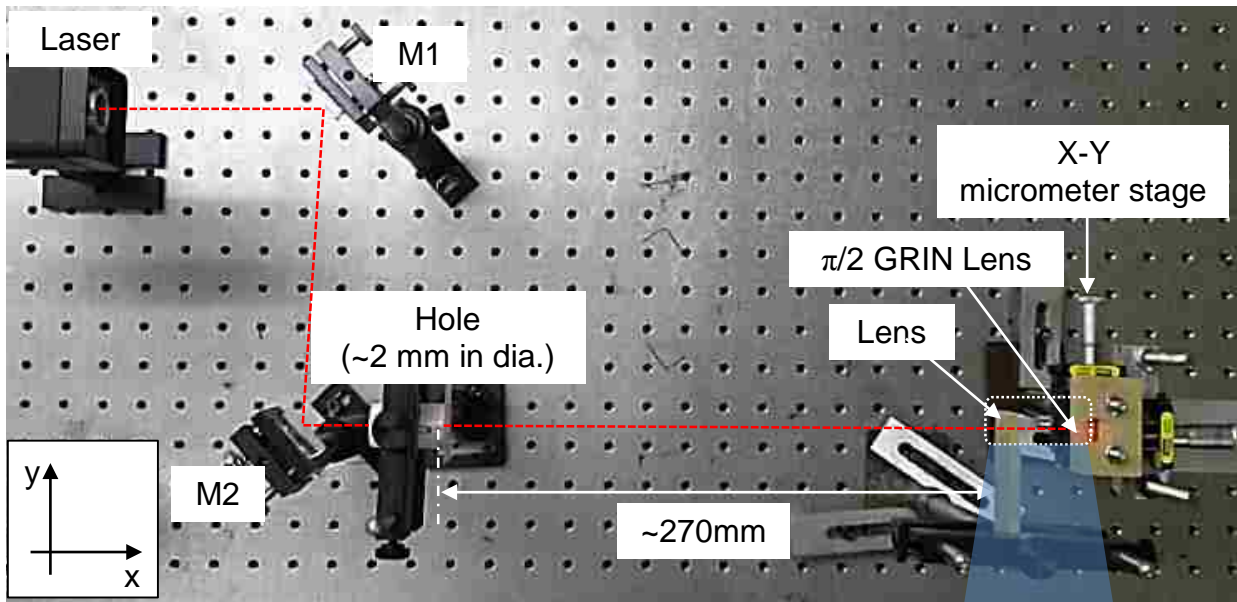


Fig. 5.5 The experimental test of the GRIN lens focusing distance depending on the epoxy thickness.



Fig. 5.6 The reflected laser beam from the gold surface makes the best focus with the distance of approximately 35.31 mm between the second lens and the first surface of GRIN lens.

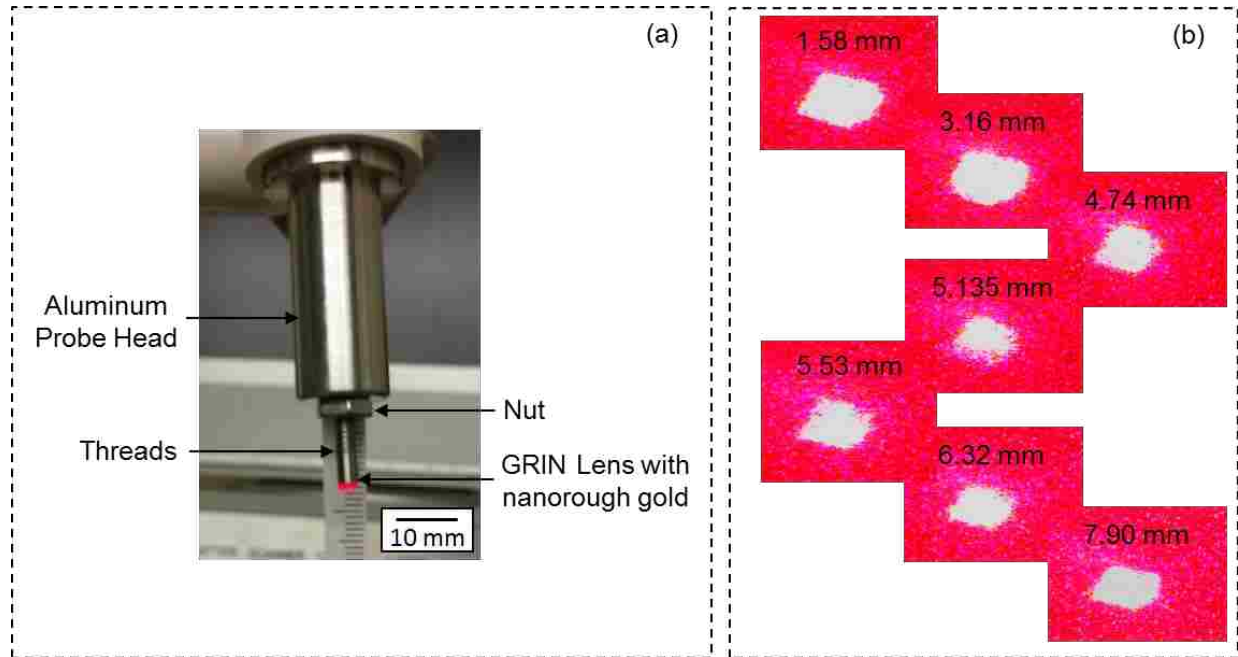


Fig. 5.7 (a) A photograph of the improved probe and (b) the laser focusing with the probe tip positons [92].

the GRIN lens is compared to numerical calculations. If a laser is illuminated through the $\pi/2$ GRIN lens in parallel, the light is focused at the other end of the GRIN lens, which is drawn in Fig. 5.8 (a). However, if the incident laser beam enters to the GRIN lens diverging, the beam passes through the GRIN lens at an angle such that, it conjugates at a point some distance away from the surface of the GRIN lens as illustrated in Fig. 5.8 (b).

Thus, a proper thickness of UV epoxy (L_{Epoxy}) can be predicted by estimating where the conjugating point (L_{Air}) is located. In this $\pi/2$ GRIN lens, the height (y) of ray trace is obtained depending on the position (x) in the lens by

$$y = \frac{\pi}{2} \cdot \frac{x}{5.2 \text{ [mm]}}$$

It is assumed that when the GRIN lens moves in x distance, the other end of the lens is positioned at $5.2 \text{ [mm]} - x$, because the light path in the GRIN lens follows sinusoidal wave. Thus, the light

traveling in $\pi/2$ GRIN lens can be predicted in two different directions depending on the media such as air on the left and UV curable epoxy on the right as shown Fig. 5.8 (b). On both sides, the light travelling out of the GRIN lens propagates with an angle which makes conjugating points.

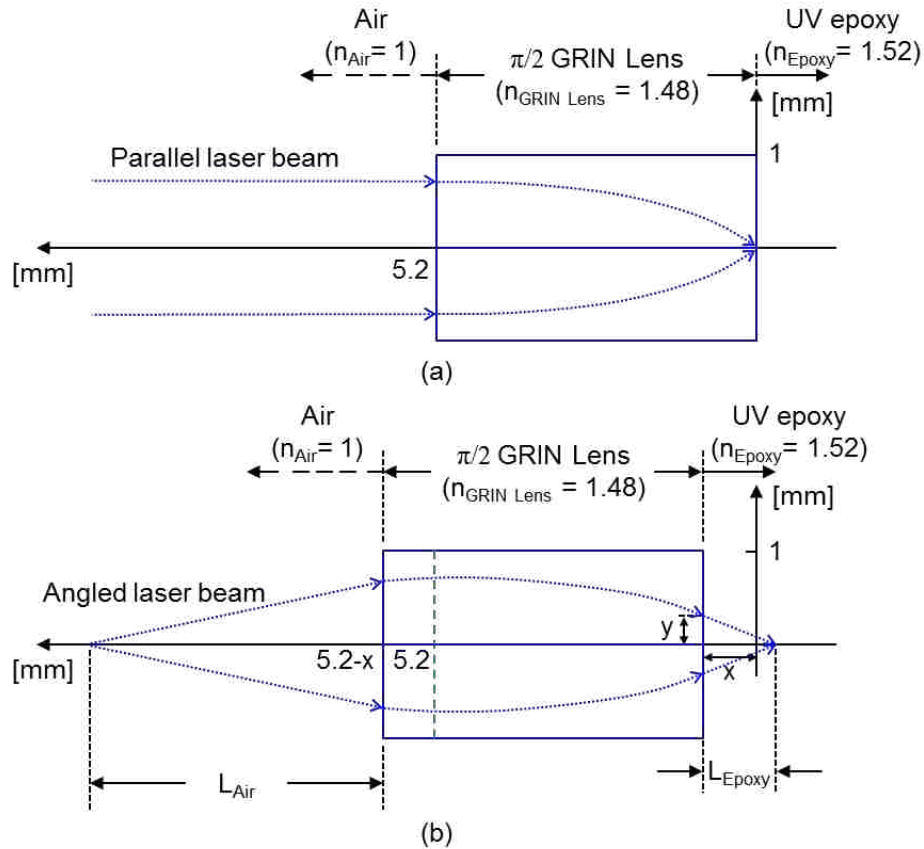


Fig. 5.8 Schematic drawing for numerical calculation of laser beam propagation in (a) parallel and (b) with a slope through $\pi/2$ GRIN Lens with 5.2 mm in length and 1 mm in radius.

The conjugate location can be calculated by the propagation slope which is obtained by the following equations:

$$y = \sin\left(\frac{\pi}{2} \cdot \frac{x}{5.2 \text{ [mm]}}\right) \text{ and}$$

$$\frac{dy}{dx} = \frac{\pi}{2} \cdot \frac{1}{5.2 \text{ [mm]}} \cos\left(\frac{\pi}{2} \cdot \frac{x}{5.2 \text{ [mm]}}\right)$$

The distances of L_{Epoxy} and L_{Air} can be obtained by using the slope as shown below

$$L_{Epoxy} = \frac{\sin\left(\frac{\pi}{2} \cdot \frac{x}{5.2 \text{ [mm]}}\right)}{dy/dx} \quad \text{and} \quad L_{Air} = \frac{\sin\left(\frac{\pi}{2} \cdot \frac{5.2 \text{ [mm]} - x}{5.2 \text{ [mm]}}\right)}{dy/dx} \times \frac{n_{Air}}{n_{GRIN \text{ Lens}}}$$

where n_{Air} and $n_{GRIN \text{ Lens}}$ are refractive index of air and GRIN lens, respectively. The factor of reflective index for L_{Epoxy} is negligible, because n_{Epoxy} and $n_{GRIN \text{ Lens}}$ are comparable. According to the equations, the probe tip position can be predicted by comparing the real epoxy thicknesses and numerical calculation shown in Fig. 5.9.

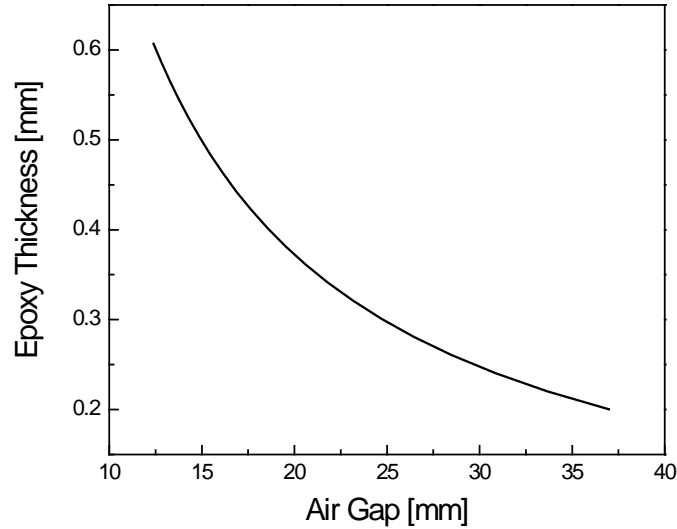


Fig. 5.9 Numerical model of epoxy thicknesses depending on the air gap.

The improved probe with external second positive lens provides more accurate focusing by increasing focusing length. About $1 \mu\text{m}$ resolution on the nanorough gold with longer $\pi/2$ GRIN lens corresponds to $100 \mu\text{m}$ displacement of GRIN lens. Therefore, the following experiment was carried out to test the new probe under the same setup of articulated arm. The probe is installed at the end of the articulated arm, and it is inserted into a block of gelatin mixed with 1 mM R6G as

displayed in Fig. 5.10 (a). The measured spectra in Fig. 5.10 (b) shows a higher signal strength than the measurement with the previous probe at the reference of 1362 cm^{-1} by a factor of 5. Multiple data points have been measured more than 1 meter from the spectrometer, and those intensities of Raman spectra were all the same.

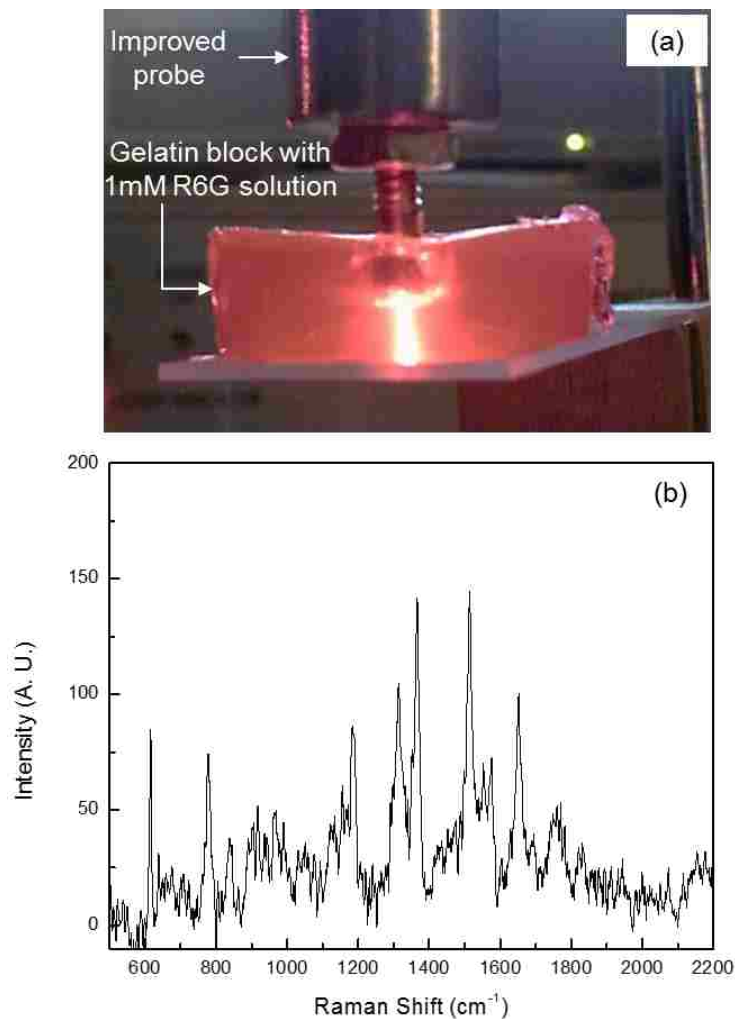


Fig. 5.10 (a) photograph of the improved probe injected into a gelatin block mixed with a 1 mM Rhodamine 6G solution, and (b) Raman spectrum of 1 mM Rhodamine 6G through the probe and the articulated arm [92].

CHAPTER 6. APPLICATIONS FOR BIOLOGICAL SPECIMEN; CHICKEN CARTILAGE

Early detection is important for most diseases. Many medical sensors and molecular imaging tools require high sensitivity and resolution for diseases. One important area for the early diagnosis is the disease in cartilage, which is a tissue that is not only flexible, but also robust. Healthy cartilage functions to protect bones from rubbing against each other, while they are in movement [93]. However, its abnormality begins from the biomolecular level, and therefore is not easily detected by change in the appearance and color. For example, if the molecular structures of the cartilage have some changes at the initial stage by a certain disease such as osteoarthritis, current molecular imaging applications including computed tomography (CT) and magnetic resonance imaging (MRI) cannot precisely detect subtle changes at the molecular level [94, 95].

Raman spectroscopy has the potential to detect even small molecular changes, since it is able to recognize individual “fingerprints” of chemical/molecular composition by inelastic light scattering. Abnormal changes in cartilage tissue can readily be detected by measuring the Raman scattering whose spectra are quite different from that of the normal cartilage. For instance, osteoarthritis (OA) is a well-known degenerative joint disease with advancing age [95, 96]. When cartilage suffers from osteoarthritis, the Raman spectra of the cartilage show similarities to the Raman signal of the bone. Normal chicken cartilage is measured under conventional Raman spectrometer with 50x microscope objective for 5 seconds integration time in this experiment, and the Raman signal is shown in Fig. 6.1 (a). The measurement is also carried out for the chicken bone under the same operating conditions of the Raman spectrometer, and the Raman spectra of the bone have a particular peak at 980 cm^{-1} which is different from the cartilage spectra (Fig. 6.1 (b).)

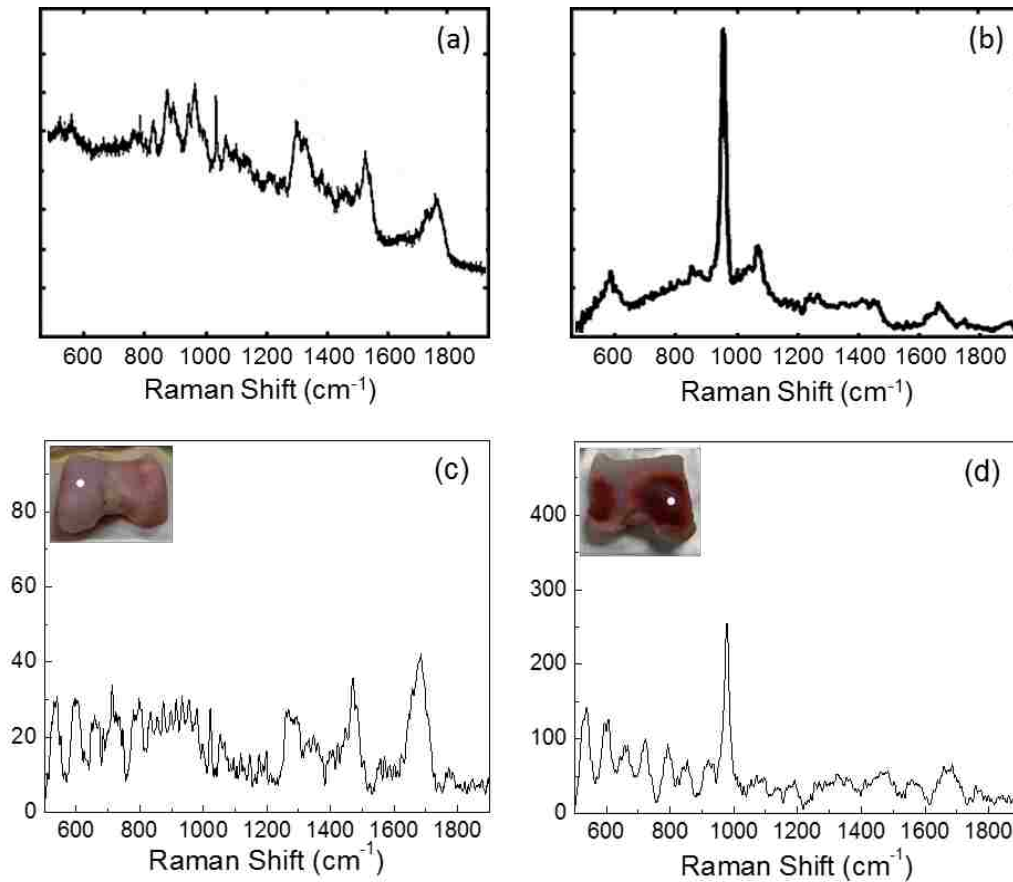


Fig. 6.1 Raman spectrum of (a) human cartilage and (b) human bone is corresponding to the measured Raman spectrum of (c) chicken cartilage and (d) chicken bone with 50x microscope objective and 5 seconds integration time [97, 98].

In addition, physical damage to cartilage is as serious as osteoarthritis disease since it may cause severe pain. There are three possible conditions: contraction, normal, and expansion of the cartilage tissues. In order to simulate these three conditions, fresh chicken cartilages were stored in three different solutions: hypertonic saline, isotonic saline and hypotonic saline overnight. In Fig. 6.2 (a), (b), and (c), Raman spectrum of the hypertonic, hypotonic, and isotonic saline are compared with conventional Raman spectrometer. Surface-Enhanced Raman Scattering (SERS) should amplify the signals, making small changes of the spectrum more distinguishable. The

possibilities of enhanced Raman scattering were tested with the conventional Raman setup, hence direct gold deposition on the cartilage is needed. However, if the gold is deposited on the cartilage which has a smooth and rough shape, it cannot be deposited uniformly over the cartilage.

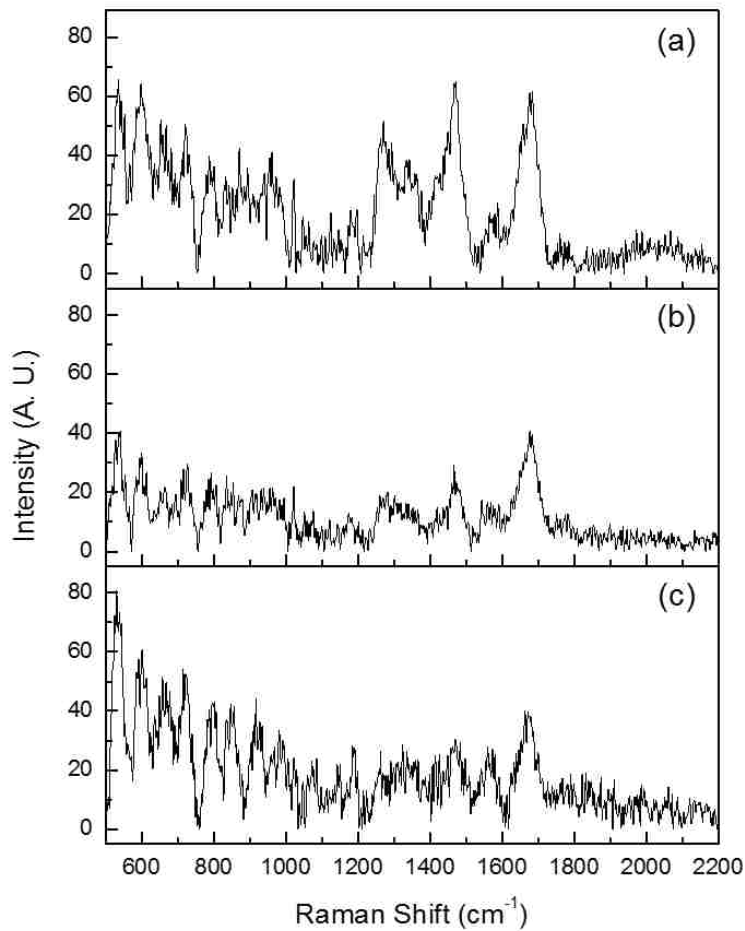


Fig. 6.2 Three cartilages are prepared with (a) hypertonic saline, (b) hypotonic saline and (c) isotonic saline, and Raman spectra are measured with 50x microscope objective and 5 seconds integration time.

Thus, chicken cartilage is sanded down from 180 grit (82 μm) to 1000 grit (10 μm) sandpaper to make a flat surface as shown in Fig. 6.3 with 440X magnification of microscope, and the gold deposition was done by sputtering. The Raman signals are compared with and without the 30 nm gold deposition in Fig. 6.4 (a) and (b), and the calculated enhancement factor is about 20. The concentration of the solid specimen cannot be changed, and therefore the calculation of the enhancement factor is different from the normal SERS enhancement calculation. The usage of the SERS can possibly contribute to the early detection with the chemical/molecular composition changes in the initial stages of osteoarthritis, because of the improved sensitivity by SERS. If

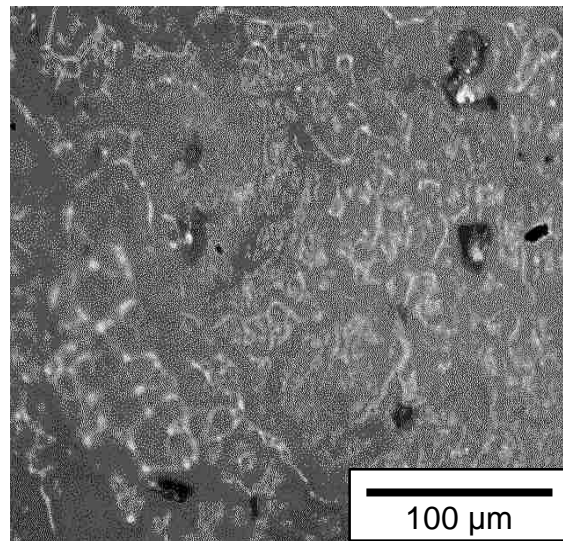


Fig. 6.3 Chicken cartilage after sanding with 10 μm grits in order to make the top surface flat.

clinical Raman probe using SERS is applied for osteoarthritis detection, it is able to perform *in-vivo* diagnosis without sample collection as required by the conventional Raman spectrometer. This is also significant because it detects whether SERS within the solid cartilage, since cartilage is a soft tissue which is very different from target samples dissolved in water for conventional Raman spectrometer.

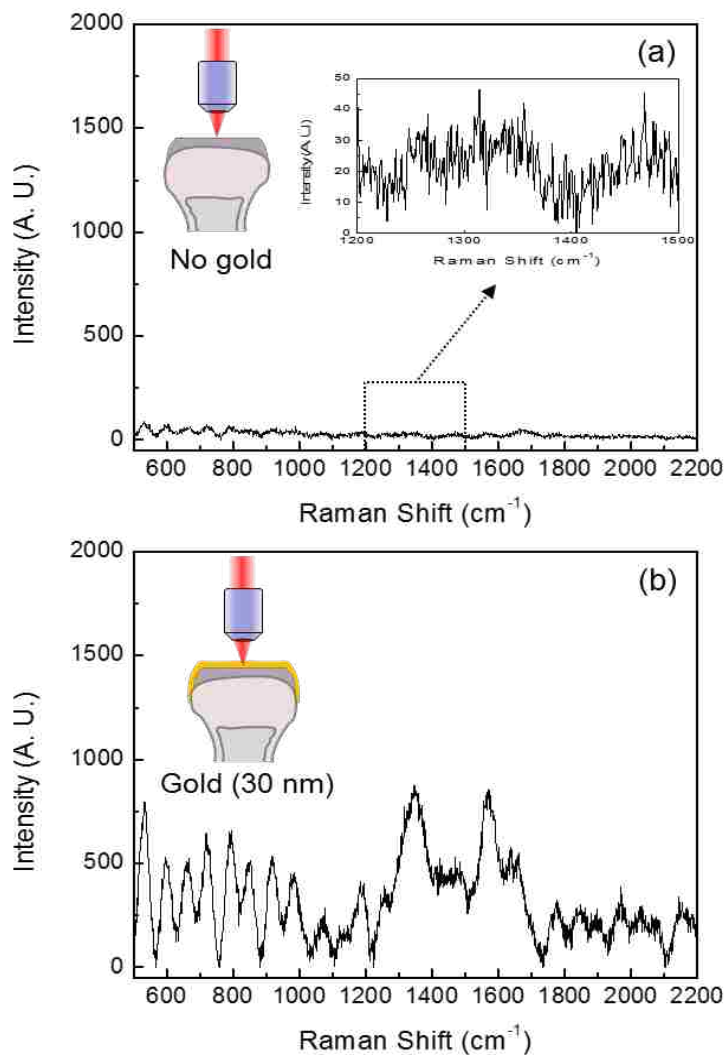


Fig. 6.4 Comparison (a) without and (b) with sputtered gold (30 nm) on sanded cartilage.

To begin the chicken cartilage detection, only the probe head is used without the articulated arm for the Raman measurement of chicken cartilage in order to check the functionality of the probe in a short distances. The cartilage stored in isotonic saline is placed on the spectrometer stage and the probe is pressed against the cartilage. The laser beam was focused at the junction between the nanorough gold and the chicken cartilage as closely as possible through the GRIN lens with sufficient pressure which left a 200 μm deep dent from on the cartilage. The short distance measurement was carried out and the Raman spectra shown in Fig. 6.5 indicates that the same signal was measured compared with the conventional Raman spectrometer, based on the five significant peaks represented with the small dots in Fig. 6.5. However, the overall signal intensities were very small although the chicken cartilage signals could be detected through the probe. It seemed that the probe was suitable for the Raman measurement, but not for the enhanced Raman signals. Thus, the Raman intensities are not sufficiently amplified, so the intensities were quite low. One possible reason for the low signal intensities is bad contact between the nanorough gold of GRIN lens and the soft chicken cartilage. Even micron spaces between the SERS substrates and the target analytes diminish a lot of signal intensities. In spite of soft tissues of chicken cartilage it might not fit into the nanorough golds like analyte solution for conventional Raman spectrometer.

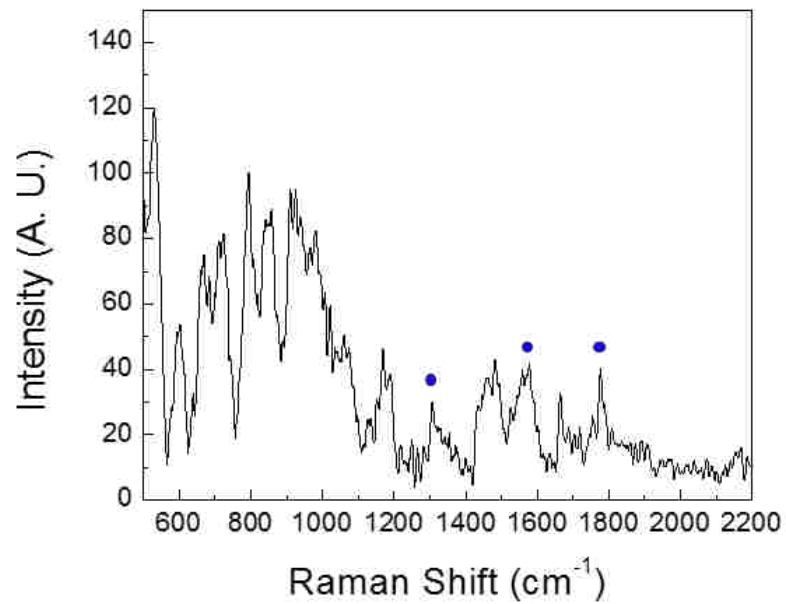


Fig. 6.5 Probe measurement with 30 nm nanorough gold against the chicken cartilage on the stage of Raman spectrometer.

CHAPTER 7. SUMMARY, CONCLUSION AND FUTURE WORK

7.1 Summary and Conclusion

A clinical Raman probe utilizing Surface-Enhanced Raman Scattering (SERS) was developed in this research as part of molecular imaging technology. A new transparent Surface-Enhanced Raman Scattering (SERS) substrate was prepared and characterized. It was assembled with an articulated arm which transmits laser light from the spectrometer to the transparent SERS substrate. One important advantage is that this probe is able to access a specimen at a remote site and the SERS effect at the end of the probe can still transmit sufficiently large Raman signals in contact with specimen.

The preparation processes of the SERS substrate are described in Fig. 6.1. A porous silicon (PS) wet etching process and reactive ion etching (RIE) dry etching process have been applied to prepare a master mold for casting transparent SERS substrates. Over each master mold, a gold layer was deposited as a releasing layer in order to facilitate the epoxy casting. Additional gold layers were also deposited on the cast rough epoxy. Raman measurements were performed within fluidic cells which was assembled with two glass microscope slides, and target solutions containing Rhodamine 6G (R6G), were injected into the cells. SERS measurement was carried out on the prepared substrates and the characteristics in reflection and transmission were compared. The characteristic analysis of SERS substrate was used for achieving the proposed concept of a prototype clinical Raman.

The prepared SERS substrate was initially attached to the glass slide working with $\pi/4$ GRIN lens for the first probe setup. The first probe was used for the remote Raman measurement with the articulated arm. For the measurement, a mixture of 1mM Rhodamine 6G (R6G) and 1g

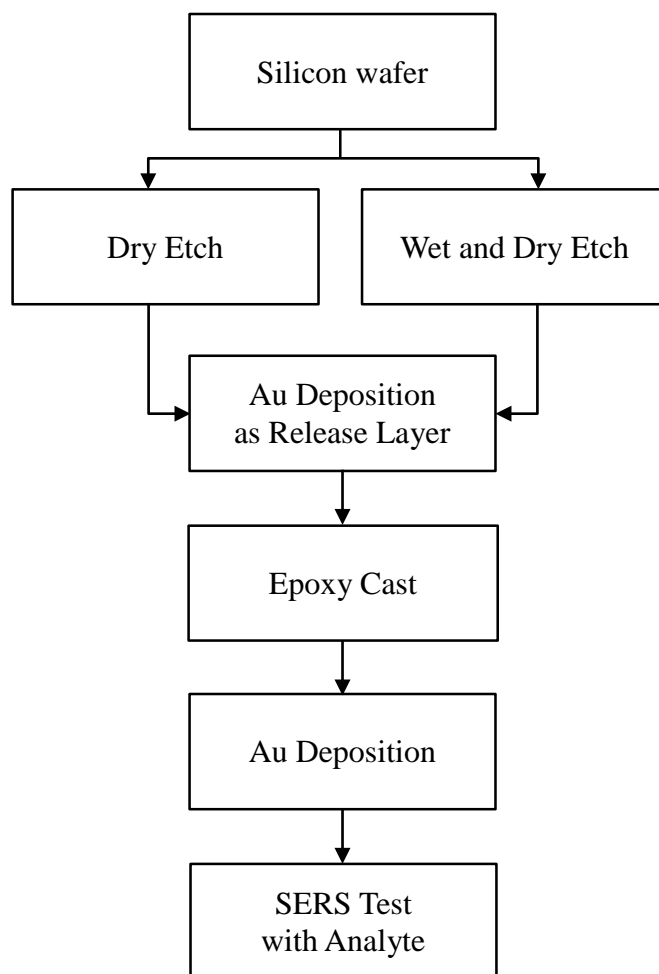


Fig. 7.1. The processing flow for the transparent SERS substrate.

of gelatin was placed more than 1 meter away from the spectrometer and the probe approached to the specimen. Lower R6G signals were measured from the remote Raman setup.

One of the disadvantages was that the probe setup could not provide fine focusing on the nanorough gold due to the low axial magnification with $\pi/4$ GRIN lens. In order to improve this weakness, a longer $\pi/2$ GRIN lens was substituted instead of the short $\pi/4$ GRIN lens. In addition

to the GRIN lens replacement, an external positive lens before the GRIN lens was inserted to provide higher axial magnification, and the best focusing distance of the GRIN lens was examined with the optical measurement setup. The focusing location of the laser beam was defined by adjusting the distance between the small positive lens and the GRIN lens. The small lens was installed in the designed aluminum housing, and the GRIN lens with SERS substrate was inserted in the stainless steel tube having a thread. Eventually, an improved probe was developed for remote Raman measurement.

Transmittance of a signal from a SERS substrate was another issue for the Raman measurement, hence the articulated arm was designed with rotating joints. The arm was composed of five rotating joints each of which has tilt mirrors, and each rotating joint was assembled with rigid pipes. Three rotating joints were able to position the probe within a 3 dimensional volume – 1 foot high x 1 foot diameter and the last two rotating joints allowed pointing the probe at any angle. Eventually, the probe was inserted into the 1 mM R6G gelatin block and demonstrated successful measurements from remote areas. In addition, the remote Raman apparatus is applied to the actual biological specimen such as a chicken cartilage so that the probe potentially can be used for osteoarthritis detection.

7.2 Future Work

Application of a remote clinical Raman probe utilizing SERS are proposed here for practical clinical usage. Clinical probes face more challenges than the enhancement of the SERS substrate and the articulated arm transmission efficiency.

Developing a SERS substrate is one challenge for collecting high signal intensities. Nanorough gold attached at the end of the probe head has presented some preliminary results against gelatin including concentration controlled R6G dye. However, it is believed that in

improved SERS substrate with a higher enhancement factor is necessary in order to detect other biomolecules such as deoxyribonucleic acid (DNA), because the 10^6 enhancement factor is relatively small compared to other published SERS substrates which reported a detectable range of DNA molecules. However, the existing probe still remains a possibility for the many clinical uses.

An articulated arm is another issue for the diminished probe efficiency from the detection areas to the spectrometer. The arm is composed of several mirrors with rotating joints and two lenses. Each mirror is normally aluminized, therefore its reflection efficiency is 89.5%. A total of five mirrors are used for the illumination to the sample, but the scattered light also passes through five mirrors in its path to the spectrometer. The scattered light intensity is much smaller than the focused laser light on the specimen. In addition, the lens does not have any treatment such as antireflection coating. Thus, the laser light intensity also decreases as it passes through the two lenses. Using multi-layered Al mirrors and anti-reflection layer coated lenses can minimize the light efficiency loss. Eventually, it can contribute to the improved performance for the clinical probe.

REFERENCES

- [1] F. C. Wong and E. E. Kim, "A review of molecular imaging studies reaching the clinical stage", *European Journal of Radiology*, 2009. 70(2): p. 205-211.
- [2] J. K. Willmann, N. van Bruggen, L. M. Dinkelborg and S. S. Gambhir, "Molecular imaging in drug development", *Nature Reviews Drug Discovery*, 2008. 7(7): p. 591-607.
- [3] T. F. Massoud and S. S. Gambhir, "Molecular imaging in living subjects: seeing fundamental biological processes in a new light", *Genes & Development*, 2003. 17(5): p. 545-580.
- [4] R. Weissleder, "Molecular imaging in cancer", *Science*, 2006. 312(5777): p. 1168-1171.
- [5] R. Weissleder and M. J. Pittet, "Imaging in the era of molecular oncology", *Nature*, 2008. 452(7187): p. 580-589.
- [6] M. L. James and S. S. Gambhir, "A molecular imaging primer: modalities, imaging agents, and applications", *Physiological Reviews*, 2012. 92(2): p. 897-965.
- [7] P. J. Cassidy and G. K. Radda, "Molecular imaging perspectives", *Journal of the Royal Society Interface*, 2005. 2(3): p. 133-144.
- [8] B. J. Pichler, H. F. Wehrl and M. S. Judenhofer, "Latest advances in molecular imaging instrumentation", *Journal of Nuclear Medicine*, 2008. 49(2) p. 5S-23S.
- [9] A. M. Blamire, "The technology of MRI--the next 10 years?", *The British Journal of Radiology*, 2008. 81(968): p. 601-617.
- [10] H. D. Liang and M. J. Blomley, "The role of ultrasound in molecular imaging", *The British Journal of Radiology*, 2003. 76(2): p. S140-150.
- [11] M. E. Phelps, "Positron emission tomography provides molecular imaging of biological processes", *Proceedings of the National Academy of Sciences*, 2000. 97(16): p. 9226-9233.
- [12] S. R. Meikle, P. Kench, M. Kassiou and R. B. Banati, "Small animal SPECT and its place in the matrix of molecular imaging technologies", *Physics in Medicine and Biology*, 2005. 50(22): p. R45-61.
- [13] M. Vendrell, K. K. Maiti, K. Dhaliwal and Y. T. Chang, "Surface-enhanced Raman scattering in cancer detection and imaging", *Trends in Biotechnology*, 2013. 31(4): p. 249-257.

- [14] C. L. Zavaleta, E. Garai, J. T. Liu, S. Sensarn, M. J. Mandella, D. Van de Sompel, S. Friedland, J. Van Dam, C. H. Contag and S. S. Gambhir, "A Raman-based endoscopic strategy for multiplexed molecular imaging", *Proceedings of the National Academy of Sciences*, 2013. 110(25): p. E2288-2297.
- [15] A. N. Garroway, P. K. Grannellx and P. Mansfield, "Image formation in NMR by a selective irradiative process", *Journal of Physics C: Solid State Physics*, 1974. 7(24): p. L457-L462.
- [16] N. Deshpande, A. Needles and J. K. Willmann, "Molecular ultrasound imaging: current status and future directions", *Clinical Radiology*, 2010. 65(7): p. 567-581.
- [17] R. Gessner and P. A. Dayton, "Advances in Molecular imaging with ultrasound", *Molecular Imaging*, 2010. 9(3): p. 117-127.
- [18] A. Rahmim and H. Zaidi, "PET versus SPECT: strengths, limitations and challenges", *Nuclear Medicine Communications*, 2008. 29(3): p. 193-207.
- [19] V. Ntziachristos, "Fluorescence molecular imaging", *Annual Review of Biomedical Engineering*, 2006. 8 p. 1-33.
- [20] B. I. Lee and J.-J. Min, "Molecular imaging using bioluminescence", *The Open Nuclear Medicine Journal*, 2010. 2(1): p. 157-165.
- [21] K. R. Zinn, T. R. Chaudhuri, A. A. Szafran, D. O'Quinn, C. Weaver, K. Dugger, D. Lamar, R. A. Kesterson, X. Wang and S. J. Frank, "Noninvasive bioluminescence imaging in small animals", *ILAR Journal*, 2008. 49(1): p. 103-115.
- [22] O. Gheysens and F. M. Mottaghy, "Method of bioluminescence imaging for molecular imaging of physiological and pathological processes", *Methods*, 2009. 48(2): p. 139-145.
- [23] C. V. Raman and K. S. Krishnan, "A new type of secondary Radiation", *Nature*, 1928. 121 p. 501-502.
- [24] E. L. Ru and P. Etchegoin, "Principles of surface-enhanced Raman spectroscopy and related plasmonic effects", 2008: Elsevier p. 688.
- [25] M. Fleischmann, P. J. Hendra and A. J. McQuillan, "Raman spectra of pyridine adsorbed at a silver electrode", *Chemical Physics Letters*, 1974. 26(2): p. 163-166.
- [26] T. Vo-Dinh, "Surface-enhanced Raman spectroscopy using metallic nanostructures", *Trends in Analytical Chemistry*, 1998. 17(8-9): p. 26.
- [27] K. J. Ling, W. S. Tse, P. Peng, S. H. Shen, K. T. Sun and S. J. Lin, "SERS in sandblast roughened metal surface", *Physica Status Solidi (a)*, 1991. 128(2): p. K123-K128.

- [28] C. D. Tran, "Subnanogram detection of dyes on filter paper by surface-enhanced Raman scattering spectrometry", *Analytical Chemistry*, 1984. 56(4): p. 824-826.
- [29] C. Jennings, R. Aroca, A. M. Hor and R. O. Loutfy, "Surface-enhanced Raman scattering from copper and zinc phthalocyanine complexes by silver and indium island films", *Analytical Chemistry*, 1984. 56(12): p. 2033-2035.
- [30] K. A. Willets and R. P. Van Duyne, "Localized surface plasmon resonance spectroscopy and sensing", *Annual Review of Physical Chemistry*, 2007. 58 p. 267-297.
- [31] J. P. Camden, J. A. Dieringer, J. Zhao and R. P. Van Duyne, "Controlled plasmonic nanostructures for surface-enhanced spectroscopy and sensing", *Accounts of Chemical Research*, 2008. 41(12): p. 1653-1661.
- [32] B. J. Kennedy, S. Spaeth, M. Dickey and K. T. Carron, "Determination of the distance dependence and experimental effects for modified SERS substrate based on self assembled monolayers formed using alkanethiols", *The Journal of Physical Chemistry B*, 1999. 103(18): p. 3640-3646.
- [33] K. Kneipp, "Surface enhanced Raman scattering", *Physics Today*, 2007. 60(11): p. 40-46.
- [34] E. C. L. Ru, E. Blackie, M. Meyer and P. G. Etchegoin, "Surface enhanced Raman scattering enhancement factors: a comprehensive study", *The Journal of Physical Chemistry C*, 2007. 111(37): p. 13794-13803.
- [35] B. Sharma, R. R. Frontiera, A.-I. Henry, E. Ringe and R. P. V. Duyne, "SERS: materials, applications, and the future", *Materials Today*, 2012. 15(1-2): p. 16-25.
- [36] R. J. C. Brown and M. J. T. Milton, "Nanostructures and nanostructured substrates for surface-enhanced Raman scattering (SERS)", *Journal of Raman Spectroscopy*, 2008. 39(10): p. 1313-1326.
- [37] S. Lin, W. Zhu, Y. Jin and K. B. Crozier, "Surface-enhanced Raman scattering with Ag nanoparticles optically trapped by a photonic crystal cavity", *Nano Letters*, 2013. 13(2): p. 559-563.
- [38] M. Wang, N. Jing, I. H. Chou, G. L. Cote and J. Kameoka, "An optofluidic device for surface enhanced Raman spectroscopy", *Lab on a Chip*, 2007. 7(5): p. 630-632.
- [39] S. Nie, "Probing Single Molecules and Single Nanoparticles by Surface-Enhanced Raman Scattering", *Science*, 1997. 275(5303): p. 1102-1106.
- [40] H. H. Wang, C. Y. Liu, S. B. Wu, N. W. Liu, C. Y. Peng, T. H. Chan, C. F. Hsu, J. K. Wang and Y. L. Wang, "Highly Raman-enhancing substrates based on silver nanoparticle arrays with tunable sub-10nm gaps", *Advanced Materials*, 2006. 18(4): p. 491-495.

- [41] R. Tantra, R. J. C. Brown and M. J. T. Milton, "Strategy to improve the reproducibility of colloidal SERS", *Journal of Raman Spectroscopy*, 2007. 38(11): p. 1469-1479.
- [42] G. L. Liu and L. P. Lee, "Nanowell surface enhanced Raman scattering arrays fabricated by soft-lithography for label-free biomolecular detections in integrated microfluidics", *Applied Physics Letters*, 2005. 87(7): p. 074101.
- [43] L. H. Qian, X. Q. Yan, T. Fujita, A. Inoue and M. W. Chen, "Surface enhanced Raman scattering of nanoporous gold: Smaller pore sizes stronger enhancements", *Applied Physics Letters*, 2007. 90(15): p. 153120.
- [44] X. N. He, Y. Gao, M. Mahjouri-Samani, P. N. Black, J. Allen, M. Mitchell, W. Xiong, Y. S. Zhou, L. Jiang and Y. F. Lu, "Surface-enhanced Raman spectroscopy using gold-coated horizontally aligned carbon nanotubes", *Nanotechnology*, 2012. 23(20): p. 205702.
- [45] T. Vo-Dinh, M. Y. K. Hiromoto, G. M. Begun and R. L. Moody, "Surface-enhanced Raman spectrometry for trace organic analysis", *Analytical Chemistry*, 1984. 56(9): p. 1667-1670.
- [46] R. P. V. Duyne, J. C. Hulthen and D. A. Treichel, "Atomic force microscopy and surface-enhanced Raman spectroscopy I Ag island films and Ag film over polymer nanosphere surfaces supported on glass", *The Journal of Chemical Physics*, 1993. 99(3): p. 2101-2115.
- [47] X. Zhang, C. R. Yonzon, M. A. Young, D. A. Stuart and R. P. Van Duyne, "Surface-enhanced Raman spectroscopy biosensors: excitation spectroscopy for optimisation of substrates fabricated by nanosphere lithography", *IEEE Proceedings Nanobiotechnology*, 2005. 152(6): p. 195-206.
- [48] R. Gordon, D. Sinton, K. L. Kavanagh and A. G. Brolo, "A new generation of sensors based on extraordinary optical transmission", *Accounts of Chemical Research*, 2008. 41(8): p. 1049-1057.
- [49] K. Sivashanmugan, J.-D. Liao, J.-W. You and C.-L. Wu, "Focused-ion-beam-fabricated Au/Ag multilayered nanorod array as SERS-active substrate for virus strain detection", *Sensors and Actuators B: Chemical*, 2013. 181 p. 361-367.
- [50] M. Kahl, E. Voges, S. Kostrewa, C. Viets and W. Hill, "Periodically structured metallic substrates for SERS", *Sensors and Actuators B: Chemical*, 1998. 51(1-3): p. 285-291.
- [51] E. J. Smythe, M. D. Dickey, J. Bao, G. M. Whitesides and F. Capasso, "Optical antenna arrays on a fiber facet for in situ surface-enhanced Raman scattering detection", *Nano Letters*, 2009. 9(3): p. 1132-1138.
- [52] W. Wu, M. Hu, F. S. Ou, Z. Li and R. S. Williams, "Cones fabricated by 3D nanoimprint lithography for highly sensitive surface enhanced Raman spectroscopy", *Nanotechnology*, 2010. 21(25): p. 255502.

- [53] C. J. Choi, Z. Xu, H. Y. Wu, G. L. Liu and B. T. Cunningham, "Surface-enhanced Raman nanodomains", *Nanotechnology*, 2010. 21(41): p. 415301.
- [54] J. D. Ryckman, M. Liscidini, J. E. Sipe and S. M. Weiss, "Direct imprinting of porous substrates: a rapid and low-cost approach for patterning porous nanomaterials", *Nano Letters*, 2011. 11(5): p. 1857-1862.
- [55] M. Rudin and R. Weissleder, "Molecular imaging in drug discovery and development", *Nature Reviews Drug Discovery*, 2003. 2(2): p. 123-131.
- [56] S. Keren, C. Zavaleta, Z. Cheng, A. de la Zerda, O. Gheysens and S. S. Gambhir, "Noninvasive molecular imaging of small living subjects using Raman spectroscopy", *Proceedings of the National Academy of Sciences*, 2008. 105(15): p. 5844-5849.
- [57] F. Giorgis, E. Descrovi, A. Chiodoni, E. Froner, M. Scarpa, A. Venturello and F. Geobaldo, "Porous silicon as efficient surface enhanced Raman scattering (SERS) substrate", *Applied Surface Science*, 2008. 254(22): p. 7494-7497.
- [58] S. Chan, S. Kwon, T.-W. Koo, L. P. Lee and A. A. Berlin, "Surface-enhanced Raman scattering of small molecules from silver-coated silicon nanopores", *Advanced Materials*, 2003. 15(19): p. 1595-1598.
- [59] K. Fukami, M. L. Chourou, R. Miyagawa, Á. Muñoz Noval, T. Sakka, M. Manso-Silván, R. J. Martín-Palma and Y. H. Ogata, "Gold nanostructures for surface-enhanced Raman spectroscopy, prepared by electrodeposition in porous silicon", *Materials*, 2011. 4(12): p. 791-800.
- [60] G. Barillaro, A. Diligenti, G. Marola and L. M. Strambini, "A silicon crystalline resistor with an adsorbing porous layer as gas sensor", *Sensors and Actuators B: Chemical*, 2005. 105(2): p. 278-282.
- [61] C. Tsamis, L. Tsoura, A. G. Nassiopoulou, A. Travlos, C. E. Salmas, K. S. Hatzilyberis and G. P. Androutopoulos, "Hydrogen catalytic oxidation reaction on Pd-doped porous silicon", *IEEE Sensors Journal*, 2002. 2(2): p. 89-95.
- [62] L. Pavesi and P. Dubos, "Random porous silicon multilayers: application to distributed Bragg reflectors and interferential Fabry - Pérót filters", *Semiconductor Science and Technology*, 1997. 12(5): p. 570-575.
- [63] M. Saadoun, H. Ezzaouia, B. Bessaïs, M. F. Boujmil and R. Bennaceur, "Formation of porous silicon for large-area silicon for large-area silicon solar cells: a new method", *Solar Energy Materials & Solar Cells*, 1999. 59(4): p. 377-385.
- [64] D. Deresme, V. Marissael, D. Stievenard and C. Ortega, "Electrical behaviour of aluminium-porous silicon junctions", *Thin Solid Films*, 1995. 255(1-2): p. 258-261.

- [65] Andreas Janshoff, Keiki-Pua S. Dancil, Claudia Steinem, Douglas P. Greiner, Victor S.-Y. Lin, Christian Gurtner, Kianoush Moteshareei, Michael J. Sailor and M. R. Ghadiri, "Macroporous p-type silicon Fabry-Perot layers. Fabrication, characterization, and applications in biosensing", *Journal of American Chemical Society*, 1998. 120 p. 12108-12116.
- [66] V. S. Lin, "A porous silicon-based optical interferometric biosensor", *Science*, 1997. 278(5339): p. 840-843.
- [67] D. R. Turner, "Electropolishing silicon in hydrofluoric acid solutions", *Journal of the Electrochemical Society*, 1958. 105(7): p. 402-408.
- [68] J. A. Uhler, "Electrolytic shaping of germanium and silicon", *The Bell System Technical Journal*, 1956. 35(2): p. 333-347.
- [69] V. Lehmann and U. Gösele, "Porous silicon formation: A quantum wire effect", *Applied Physics Letters*, 1991. 58(8): p. 856-858.
- [70] X. G. Zhang, "Morphology and formation mechanisms of porous silicon", *Journal of The Electrochemical Society*, 2004. 151(1): p. C69.
- [71] T. Urata, K. Fukami, T. Sakka and Y. H. Ogata, "Pore formation in p-type silicon in solutions in containing different types of alcohol", *Nanoscale Research Letters*, 2012. 7(1): p. 5.
- [72] S. Lazarouk, P. Jaguiro, S. Katsouba, G. Maiello, S. L. Monica, G. Masini, E. Proverbio and A. Ferrari, "Visual determination of thickness and porosity of porous silicon layers", *Thin Solid Films*, 1997. 297(1-2): p. 97-101.
- [73] W. R. Ashurst, C. Carraro, R. Maboudian and W. Frey, "Wafer level anti-stiction coatings for MEMS", *Sensors and Actuators A: Physical*, 2003. 104(3): p. 213-221.
- [74] D. R. Barbero, M. S. M. Saifullah, P. Hoffmann, H. J. Mathieu, D. Anderson, G. A. C. Jones, M. E. Welland and U. Steiner, "High-resolution nanoimprinting with a robust and reusable polymer mold", *Advanced Functional Materials*, 2007. 17(14): p. 2419-2425.
- [75] W. R. Ashurst, C. Carraro and R. Maboudian, "Vapor phase anti-stiction coating for MEMS", *IEEE Transactions on Device and Materials Reliability*, 2003. 3(4): p. 173-178.
- [76] I. M. White, S. H. Yazdi and W. W. Yu, "Optofluidic SERS: synergizing photonics and microfluidics for chemical and biological analysis", *Microfluidics and Nanofluidics*, 2012. 13(2): p. 205-216.
- [77] J. Kim, K. N. Kang, A. Sarkar, P. Malempati, D. Hah, T. Daniels-Race and M. Feldman, "Nanorough gold for enhanced Raman scattering", *Journal of Vacuum Science & Technology B*, 2013. 31(6): p. 6FE02.

- [78] M. Bele, "Preparation and flow cytometry of uniform silica-fluorescent dye microspheres", *Journal of Colloid and Interface Science*, 2002. 254(2): p. 274-282.
- [79] M. Frankowski, J. Theisen, A. Kummrow, P. Simon, H. Ragusch, N. Bock, M. Schmidt and J. Neukammer, "Microflow cytometers with integrated hydrodynamic focusing", *Sensors (Basel)*, 2013. 13(4): p. 4674-4693.
- [80] E. Sherman, A. Itkin, Y. Y. Kuttner, E. Rhoades, D. Amir, E. Haas and G. Haran, "Using fluorescence correlation spectroscopy to study conformational changes in denatured proteins", *Biophysical Journal*, 2008. 94(12): p. 4819-4827.
- [81] A. Casoli and M. Schönhoff, "Fluorescence correlation spectroscopy as a tool to investigate single molecule probe dynamics in thin polymer films", *Biological Chemistry*, 2001. 382(3): p. 363-369.
- [82] J.-H. Wang, J. D. Bartlett, A. C. Dunn, S. Small, S. L. Willis, M. J. Driver and A. L. Lewis, "The use of rhodamine 6G and fluorescence microscopy in the evaluation of phospholipid-based polymeric biomaterials", *Journal of Microscopy*, 2005. 217(3): p. 216-224.
- [83] S. W. Hell, K. Bahlmann, M. Schrader, A. Soini, H. Malak, I. Gryczynski and J. R. Lakowicz, "Three-photon excitation in fluorescence microscopy", *Journal of Biomedical Optics*, 1996. 1(1): p. 71-74.
- [84] D. Lutic, C. Coromelci-Pastravanu, I. Cretescu, I. Poullos and C.-D. Stan, "Photocatalytic treatment of rhodamine 6G in wastewater using photoactive ZnO", *International Journal of Photoenergy*, 2012. 2012: p. 1-8.
- [85] Y.-C. Yang, T.-K. Huang, Y.-L. Chen, J.-Y. Mevellec, S. Lefrant, C.-Y. Lee and H.-T. Chiu, "Electrochemical growth of gold nanostructures for surface-enhanced Raman scattering", *The Journal of Physical Chemistry C*, 2011. 115(5): p. 1932-1939.
- [86] J. Rose, S. Pacelli, A. Haj, H. Dua, A. Hopkinson, L. White and F. Rose, "Gelatin-based materials in ocular tissue engineering", *Materials*, 2014. 7(4): p. 3106-3135.
- [87] J. M. Bello, V. A. Narayanan, D. L. Stokes and T. Vo-Dinh, "Fiber-optic remote sensor for in situ surface-enhanced Raman scattering analysis", *Analytical Chemistry*, 1990. 62(22): p. 2437-2441.
- [88] Richard L. McCreery, Martin Fleischmann and P. Hendra, "Fiber optic probe for remote raman spectrometry", *Analytical Chemistry*, 1983. 55(1): p. 146-148.
- [89] Y. Komachi, H. Sato, K. Aizawa and H. Tashiro, "Micro-optical fiber probe for use in an intravascular Raman endoscope", *Applied Optics*, 2005. 44(22): p. 4722-4732.
- [90] S. Pålsson, "Development of a fiber-optical probe for near-infrared Raman spectroscopy in tissue", Master's Thesis, Lund University, Lund, Sweden, 1997.

- [91] Y. Matsuura, S. Kino, E. Yokoyama, T. Katagiri, H. Sato and H. Tashir, "Flexible fiber-optics probes for Raman and FT-IR remote spectroscopy", *IEEE Journal of Selected Topics in Quantum Electronics*, 2007. 13(6): p. 1704-1708.
- [92] J. Kim, D. Hah, T. Daniels-Race and M. Feldman, "Clinical probe utilizing surface enhanced Raman scattering", *Journal of Vacuum Science & Technology B*, 2014. 32(6): p. 06FD02.
- [93] P. T. Paradowski, "Osteoarthritis of the knee: Assessing the disease", *Health Care: Current Reviews*, 2014. 2(2): p. e103.
- [94] A. Guermazi, F. W. Roemer, D. Burstein and D. Hayashi, "Why radiography should no longer be considered a surrogate outcome measure for longitudinal assessment of cartilage in knee osteoarthritis", *Arthritis Research & Therapy*, 2011. 13(6): p. 247.
- [95] I. Haq, E. Murphy and J. Dacre, "Osteoarthritis", *Postgraduate Medical Journal*, 2003. 79(933): p. 377-383.
- [96] Y. Zhang and J. M. Jordan, "Epidemiology of osteoarthritis", *Clin Geriatr Med*, 2010. 26(3): p. 355-369.
- [97] Y. Takahashi, N. Sugano, M. Takao, T. Sakai, T. Nishii and G. Pezzotti, "Raman spectroscopy investigation of load-assisted microstructural alterations in human knee cartilage: Preliminary study into diagnostic potential for osteoarthritis", *Journal of the Mechanical Behavior of Biomedical Materials*, 2014. 31 p. 77-85.
- [98] A. Carden, R. M. Rajachar, M. D. Morris and D. H. Kohn, "Ultrastructural changes accompanying the mechanical deformation of bone tissue: a Raman imaging study", *Calcif Tissue Int*, 2003. 72(2): p. 166-175.

APPENDIX A. PERMISSION TO REPRINT COPYRIGHTED MATERIAL

AIP PUBLISHING LLC LICENSE TERMS AND CONDITIONS

Jun 23, 2015

All payments must be made in full to CCC. For payment instructions, please see information listed at the bottom of this form.

License Number	3654590372191
Order Date	Jun 23, 2015
Publisher	AIP Publishing LLC
Publication	Journal of Vacuum Science & Technology B
Article Title	Nanorough gold for enhanced Raman scattering
Author	Jeonghwan Kim, Kyung-Nam Kang, Anirban Sarkar, et al.
Online Publication Date	Oct 29, 2013
Volume number	31
Issue number	6
Type of Use	Thesis/Dissertation
Requestor type	Author (original article)
Format	Electronic
Portion	Figure/Table
Number of figures/tables	8
Title of your thesis / dissertation	CLINICAL PROBE UTILIZING SURFACE-ENHANCED RAMAN SCATTERING (SERS) FOR IN-SITU MOLECULAR IMAGING APPLICATIONS
Expected completion date	Aug 2015
Estimated size (number of pages)	114

APPENDIX B. PERMISSION TO REPRINT COPYRIGHTED MATERIAL

AIP PUBLISHING LLC LICENSE TERMS AND CONDITIONS

Jun 23, 2015

All payments must be made in full to CCC. For payment instructions, please see information listed at the bottom of this form.

License Number	3654590551498
Order Date	Jun 23, 2015
Publisher	AIP Publishing LLC
Publication	Journal of Vacuum Science & Technology B
Article Title	Clinical probe utilizing surface enhanced Raman scattering
Author	Jeonghwan Kim,Dooyoung Hah,Theda Daniels-Race, et al.
Online Publication Date	Sep 26, 2014
Volume number	32
Issue number	6
Type of Use	Thesis/Dissertation
Requestor type	Author (original article)
Format	Electronic
Portion	Figure/Table
Number of figures/tables	2
Title of your thesis / dissertation	CLINICAL PROBE UTILIZING SURFACE-ENHANCED RAMAN SCATTERING (SERS) FOR IN-SITU MOLECULAR IMAGING APPLICATIONS
Expected completion date	Aug 2015
Estimated size (number of pages)	114
Total	0.00 USD

APPENDIX C. PERMISSION TO REPRINT COPYRIGHTED MATERIAL

ELSEVIER LICENSE TERMS AND CONDITIONS

Jul 02, 2015

This is a License Agreement between Jeonghwan Kim ("You") and Elsevier ("Elsevier") provided by Copyright Clearance Center ("CCC"). The license consists of your order details, the terms and conditions provided by Elsevier, and the payment terms and conditions.

All payments must be made in full to CCC. For payment instructions, please see information listed at the bottom of this form.

Supplier	Elsevier Limited The Boulevard, Langford Lane Kidlington, Oxford, OX5 1GB, UK
Registered Company Number	1982084
Customer name	Jeonghwan Kim
License number	3633110311822
License date	May 20, 2015
Licensed content publisher	Elsevier
Licensed content publication	Journal of the Mechanical Behavior of Biomedical Materials
Licensed content title	Raman spectroscopy investigation of load-assisted microstructural alterations in human knee cartilage: Preliminary study into diagnostic potential for osteoarthritis
Licensed content author	Yasuhiro Takahashi, Nobuhiko Sugano, Masaki Takao, Takashi Sakai, Takashi Nishii, Giuseppe Pezzotti
Licensed content date	March 2014
Licensed content volume number	31
Licensed content issue number	n/a
Type of Use	reuse in a thesis/dissertation
Portion	figures/tables/illustrations
Number of figures/tables/illustrations	1
Format	both print and electronic
Are you the author of this Elsevier article?	No
Will you be translating?	No
Original figure numbers	figure 2-a
Title of your thesis/dissertation	CLINICAL PROBE UTILIZING SURFACE-ENHANCED RAMAN SCATTERING (SERS) FOR IN-SITU MOLECULAR IMAGING APPLICATIONS
Expected completion date	Aug 2015
Estimated size (number of pages)	114
Elsevier VAT number	GB 494 6272 12

APPENDIX D. PERMISSION TO REPRINT COPYRIGHTED MATERIAL

SPRINGER LICENSE TERMS AND CONDITIONS

Jun 22, 2015

This is a License Agreement between Jeonghwan Kim ("You") and Springer ("Springer") provided by Copyright Clearance Center ("CCC"). The license consists of your order details, the terms and conditions provided by Springer, and the payment terms and conditions.

All payments must be made in full to CCC. For payment instructions, please see information listed at the bottom of this form.

License Number	3633110596140
License date	May 20, 2015
Licensed content publisher	Springer
Licensed content publication	Calcified Tissue International
Licensed content title	Ultrastructural Changes Accompanying the Mechanical Deformation of Bone Tissue: A Raman Imaging Study
Licensed content author	A. Carden
Licensed content date	Dec 31, 1969
Volume number	72
Issue number	2
Type of Use	Thesis/Dissertation
Portion	Figures
Author of this Springer article	No
Order reference number	None
Original figure numbers	figure 2-B
Title of your thesis / dissertation	CLINICAL PROBE UTILIZING SURFACE-ENHANCED RAMAN SCATTERING (SERS) FOR IN-SITU MOLECULAR IMAGING APPLICATIONS
Expected completion date	Aug 2015
Estimated size(pages)	114
Total	0.00 USD

VITA

Jeonghwan Kim was born in Busan, South Korea in 1980. He graduated with his Bachelor of Engineering (B.Eng.) degree in 2007 in Electronic Engineering from Kyungwon University (Now Known As Gachon University), S. Korea. Since 2009, he joined at Louisiana State University (LSU), Baton Rouge, Louisiana for his graduate study in the Division of Electrical & Computer Engineering. In 2011, he earned his Master of Science (M.S.) degree under Dr. Pratul K. Ajmera from Louisiana State University with the topic of hydrodynamic focusing micropump module with PDMS/nickel-particle composite diaphragms for microfluidic systems. He was interested in MEMS technologies merged with nanophotonics and applied optics. He started his Ph.D. research “clinical probe utilizing Surface-Enhanced Raman Scattering (SERS) for in-situ molecular imaging applications” under Dr. Dooyoung Hah until Dr. Hah left LSU. His Ph.D. research was kept up with Dr. Marin Feldman until he earns Ph.D. degree.